The hydrodynamic evolution of binary black holes embedded within the vertically stratified disks of active galactic nuclei

Nicholas Kaaz,[1,2] Sophie Lund Schrøder,[3] Jeff J. Andrews,[2] Andrea Antoni,[4] and Enrico Ramirez-Ruiz[5,3]

[1]*Department of Physics & Astronomy, Northwestern University, Evanston, IL 60202, USA*
[2]*Center for Interdisciplinary Exploration & Research in Astrophysics (CIERA), Evanston, IL 60202, USA*
[3]*Niels Bohr Institute, University of Copenhagen, Blegdamsvej 17, DK-2100 Copenhagen, Denmark*
[4]*Department of Astronomy, University of California, Berkeley, CA 94720, USA*
[5]*Department of Astronomy & Astrophysics, University of California, Santa Cruz, CA 95064, USA*

ABSTRACT

Stellar-mass black holes can become embedded within the gaseous disks of active galactic nuclei (AGNs). Afterwards, their interactions are mediated by their gaseous surroundings. In this work, we study the evolution of stellar-mass binary black holes (BBHs) embedded within AGN disks using a combination of three-dimensional hydrodynamic simulations and analytic methods, focusing on environments in which the AGN disk scale height H is $\gtrsim$ the BBH sphere of influence. We model the local surroundings of the embedded BBHs using a wind tunnel formalism and characterize different accretion regimes based on the local properties of the disk, which range from wind-dominated to quasi-spherical. We use our simulations to develop prescriptions for mass accretion and drag for embedded BBHs. We use these prescriptions, along with AGN disk models that can represent the Toomre-unstable outer regions of AGN disks, to study the long-term evolution of the BBHs as they migrate through the disk. We find that BBHs typically merge within $\lesssim 5-30\,\mathrm{Myr}$, increasing their mass significantly in the process, allowing BBHs to enter (or cross) the pair-instability supernova mass gap. The rate at which gas is supplied to these BBHs often exceeds the Eddington limit, sometimes by several orders of magnitude. We conclude that most embedded BBHs will merge before migrating significantly in the disk. Depending on the conditions of the ambient gas and the distance to the system, LISA can detect the transition between the gas-dominated and gravitational wave dominated regime for inspiraling BBHs that are formed sufficiently close to the AGN ($\lesssim 0.1$ pc). We also discuss possible electromagnetic signatures during and following the inspiral, finding that it is generally unlikely but not inconceivable for the bolometric luminosity of the BBH to exceed that of the host AGN.

1. INTRODUCTION

Direct observations of Sagittarius A*, the supermassive black hole (SMBH) at the center of our galaxy, indicate the existence of a population of massive stars within its sphere of influence (Schödel et al. 2002; Ghez et al. 2003; Paumard et al. 2006; Lu et al. 2009; Bartko et al. 2009, 2010). Furthermore, the growing observational sample of tidal disruption events suggests that relatively young stellar populations are ubiquitous around SMBHs (Law-Smith et al. 2017; French et al. 2020; Mockler & Ramirez-Ruiz 2021). While most active galactic nuclei (AGN) harbor SMBHs with low accretion rates (Ptak 2001), a subset of AGN are commonly believed to harbor accretion disks that are abundant in cold, dense gas (Heckman & Best 2014). These disks remain 'canonically' thin (Shakura & Sunyaev 1973) up to scales of $10^{-2} - 1$ pc (Sirko & Goodman 2003) depending on the mass of the

SMBH, and at larger radii gradually transition between the gas-dominated accretion disk and the star-dominated galactic disk.

It has recently been realized that a subset of the stars around AGN comprise massive stellar binaries that evolve into binary BHs (BBHs). Over the past several years LIGO/Virgo has detected dozens of BBHs mergers (Abbott et al. 2019; The LIGO Scientific Collaboration et al. 2020; Abbott et al. 2020a) which are typically attributed to formation through isolated binary evolution (Belczynski et al. 2016; Giacobbo & Mapelli 2018; Kruckow et al. 2018; Schrøder et al. 2018; Bavera et al. 2020) or dynamical interactions in dense stellar systems (O'Leary et al. 2009; Antonini & Perets 2012; Samsing et al. 2014; Antonini et al. 2017; Askar et al. 2017; Samsing & Ramirez-Ruiz 2017; Banerjee 2018; Fragione & Kocsis 2018; Rodriguez et al. 2018; Samsing & D'Orazio 2018; Kremer et al. 2018, 2019; Di Carlo et al. 2019). However, a potentially significant fraction of all LIGO/Virgo events may be due to BBHs that merge within an AGN disk (McKernan et al. 2012, 2014;

Corresponding author: Nicholas Kaaz
nkaaz@u.northwestern.edu

Bartos et al. 2017; Stone et al. 2017; Tagawa et al. 2019).
Due to the high gas densities within the disk, accretion and
gas drag will help the binary inspiral much faster than via
three-body hardening and gravitational wave emission alone
(Antoni et al. 2019).

The possibility that BBHs may merge within an AGN disk
provides the tantalizing prospect that some BBH mergers
may produce an associated electromagnetic (EM) counter-
part; at the moment of merger, the sudden mass loss and
recoil of the product black hole (BH) may shock-heat the
surrounding accretion flow, resulting in an optical/UV flare
(Lippai et al. 2008; Corrales et al. 2010; de Mink & King
2017; McKernan et al. 2019). While largely unproven, this
scenario was reinvigorated with the recently claimed asso-
ciation of the BBH merger GW190521 with an AGN flare
(Graham et al. 2020), although we note that the significance
of this association has been questioned (Ashton et al. 2020).
This scenario is particularly intriguing because the BHs that
merged to generate GW190521 are sufficiently massive that
they fall within the pair-instability supernova (PISN) mass
gap (Abbott et al. 2020b), suggesting that GW190521 could
not have been formed through standard binary evolution sce-
narios (Safarzadeh et al. 2020a,b; Vigna-Gómez et al. 2021)
unless our understanding of PISN is in significant error (e.g.,
Belczynski 2020). It is therefore worth exploring the pos-
sibility that certain BBH mergers, such as GW190521, may
have been formed in an AGN disk.

Stellar-mass BBHs can end up orbiting in the midplane of
an AGN disk via two methods. First, they can form *in situ*: in
the outer reaches of AGN disks, the gas becomes Toomre un-
stable, forming generations of stars already embedded within
the disk (Toomre 1964; Goodman 2003). The BHs that are
birthed by this generation of stars couple to the surrounding
gaseous disk and stellar population, causing them to inspiral
towards the central SMBH - and, in the case of binary sys-
tems, cause their orbital separation to shrink (e.g., Stone et al.
2017). Second, black holes can form in the surrounding nu-
clear cluster then migrate into the AGN disk via dynamical
interactions: the density of the nuclear cluster is sufficiently
high that its most massive constituents - the black holes - will
mass segregate into the central regions, nearest the SMBH
(Morris 1993; Rasio et al. 2004). Here, the gravitational in-
fluence of the AGN disk is strong, and the mass-segregated
black holes will gradually have their inclinations and eccen-
tricities damped until they occupy circular orbits embedded
within the AGN disk (Ward & Hahn 1994; Tanaka & Ward
2004). Single, rather than binary, BHs may also become em-
bedded by these same mechanisms and then efficiently pair
up via gas-mediated single-single encounters (Tagawa et al.
2019).

Once embedded within the AGN disk, BBH evolution is
driven by a combination of three-body and hydrodynamic in-
teractions. Repeated single-double encounters increasingly
harden binaries. It is estimated that within $\lesssim 10$ encounters,
a BBH can be sufficiently hardened such that gravitational
waves can merge the binary within a Hubble time (Leigh
et al. 2018). At the same time, gaseous torques from the disk
influence the center-of-mass motion of the BBH. Depend-
ing on the assumed AGN disk profile, these gaseous torques
can be negative far from the SMBH and positive close to the
SMBH, causing embedded objects to become stuck in 'mi-
gration traps' (Lyra et al. 2010; Paardekooper et al. 2010,
2011). Within a populated migration trap, the rate of BH and
BBH interactions are increased, potentially leading to rapid
merger times (Secunda et al. 2019, 2020).

In these models, a critical ingredient is gas drag that ex-
erts negative torques on the binary that help it inspiral on
short timescales. Typically, this effect is included using
semi-analytic prescriptions (Tagawa et al. 2016; Tagawa &
Umemura 2018; McKernan et al. 2018). These prescriptions
are often motivated by more detailed hydrodynamic simula-
tions of accreting binaries (e.g., Antoni et al. 2019), yet hy-
drodynamic studies of embedded BBHs remain rare. Notable
exceptions include Baruteau et al. (2011) and more recently
Li et al. (2021), who both simulated the two-dimensional hy-
drodynamic evolution of the AGN disk coupled with the or-
bital evolution of the embedded BBH. However, these works
focused on large mass ratios (appropriate for $\lesssim 10^6 - 10^7 M_\odot$
SMBHs) and thin AGN disks. For heavier ($\gtrsim 10^7 M_\odot$)
SMBHs or thicker AGN disks, the disk scale height can very
well be larger than the BBH sphere of influence, making the
accretion flow inherently three-dimensional.

In this work, we study the properties of the accretion flow
surrounding embedded BBHs in vertically stratified AGN
disks and explore its consequences on their long-term evolu-
tion. In Section 2, we consider the flow geometry surround-
ing embedded BBHs and contextualize them within AGN
disk models. We describe our numerical method and present
the results of our hydrodynamic simulations in Section 3. We
apply these results in Section 4, where we study the long-
term evolutionary tracks of embedded BBHs as they migrate
through the host disk. Finally, in Section 5 we discuss the im-
plications of our results for gravitational-wave sources, pos-
sible electromagnetic signatures, potential caveats and then
provide a summary of our findings.

2. SETTING THE STAGE

2.1. *Characteristic scales*

Consider a BBH that is embedded within an AGN disk.
Assume the center of mass of the binary occupies a circular
orbit at distance D from the SMBH and assume the center
of mass corotates with the disk. Disk annuli closer to the
SMBH will orbit faster than the BBH, and annuli farther from
the SMBH will orbit slower. In the rest-frame of the BBH,
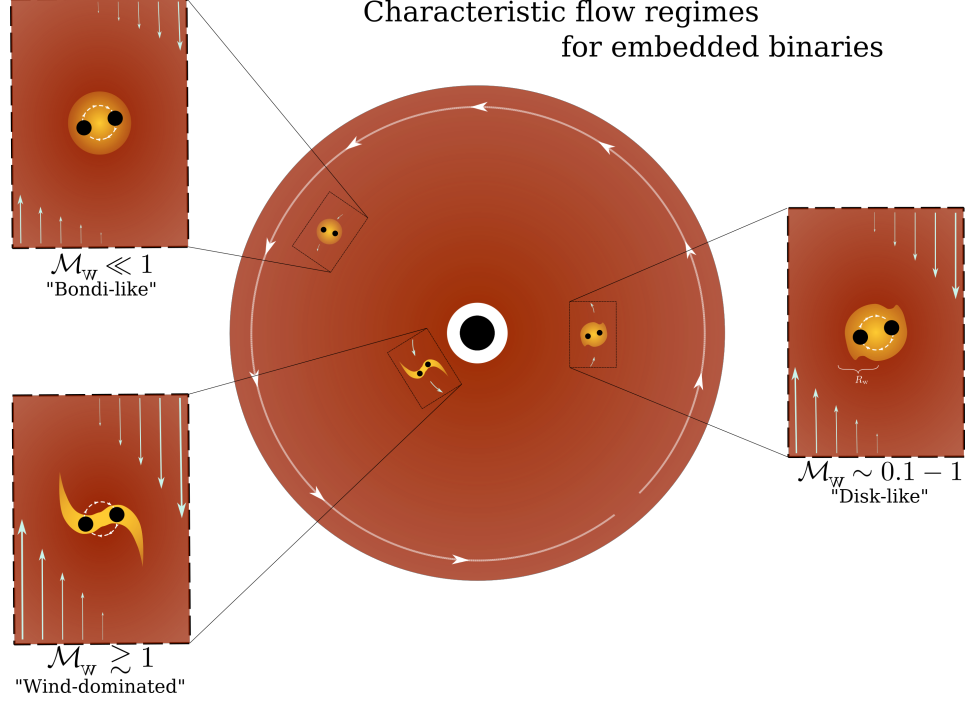
Figure 1. Here, we present a cartoon depiction of the three regimes that we use to describe embedded black hole binaries. We remind the reader that this framework is valid for vertically stratified, three-dimensional accretion flows, but at large $\mathcal{M}_w$, H becomes much smaller than the BBH sphere of influence, and the flow geometry becomes planar. The rectangular inset drawings represent the "wind tunnel" computational domain that we use in our simulations. **Upper left:** Far from the central SMBH, the binary sees little of the disk velocity gradient, and accretes in a quasi-spherical Bondi-like fashion. **Lower left:** Binaries that live near their host SMBH struggle to accrete from the high-velocity disk wind, and gas pressure is unable to thermalize incident streamlines. **Center right:** For binaries at intermediate distances from the SMBH, the AGN disk deposits angular momentum into the flow, creating structures with partial centrifugal support.

this results in a shearing wind that engulfs the binary. Within some sphere of influence, the BBH will feed from the AGN disk, accreting both mass and angular momentum. The two relevant length scales are the Hill radius of the BBH,

$$R_H = D \left(\frac{q}{3}\right)^{1/3}, \tag{1}$$

where D is the distance from the SMBH to the BBH center of mass, and $q = M/M_{SMBH}$ is the BBH-SMBH mass ratio. The second length scale to consider is the Bondi radius,

$$R_b = \frac{GM}{c_s^2}, \tag{2}$$

were c_s is the local sound speed at distance D in the disk. At radii larger than R_b, the pressure support of the gas allows it to be unperturbed by the gravity of the BBH. The sphere of influence of the BBH will be limited by the smaller of these two length-scales. If $R_H < R_b$, the ram pressure of the wind is more important than the gas pressure, and if $R_b < R_H$ the opposite is true. To parameterize the relative strength of these two regimes, we start by writing down the velocity profile of the wind in the BBH rest frame,

$$v(\delta r) = v_k(D + \delta r) - v_k(D), \tag{3}$$

where v_k is the Keplerian velocity and δr is the relative distance from the BBH. It's advantageous to linearize this velocity profile because it will later allow us to model embedded BBHs in a scale-free fashion,

$$v(\delta r) \approx -\frac{1}{2}\delta r \Omega_k, \tag{4}$$

where $\Omega_k = \sqrt{\frac{GM_{SMBH}}{D^3}}$ is the Keplerian frequency about the SMBH. The sphere of influence of the BBH is always limited by R_H, and at this radius the linearized velocity deviates only marginally from the true velocity when $q \ll 1$. We define the 'wind-capture radius', R_w, as the radius at which a wind with the linearized velocity profile $v(\delta r)$ is marginally bound to the BBH,

$$R_w \equiv \frac{2GM}{v(R_w)^2} = 2Dq^{1/3} \tag{5}$$

This quantity differs from the Hill radius only by a constant, i.e. $R_w = 24^{1/3}R_H$. Using Equation 4 with $\delta r = R_w$, we define the Mach number of the wind at the wind-capture radius as,

$$\mathcal{M}_w \equiv \frac{\Omega_k R_w}{2c_s}. \tag{6}$$

Using the relation $H/R = c_s/v_k$ (Pringle 1981), where H/R is the disk aspect ratio, we can rewrite this expression as,

$$\mathcal{M}_w = q^{1/3}(H/R)^{-1}. \tag{7}$$

We have found that our accretion flow is most strongly dictated by $\mathcal{M}_\mathrm{w}$. This is illustrated in Figure 1, where we delineate three flow regimes defined by $\mathcal{M}_\mathrm{w}$. When $\mathcal{M}_\mathrm{w} \ll 1$, then $R_\mathrm{b} \ll R_\mathrm{H}$, and the flow accretes in a quasi-spherical, Bondi-like fashion. When $\mathcal{M}_\mathrm{w} > 1$, then the wind flowing through the BBH's sphere of influence is supersonic, and has high specific angular momentum. Here, the flow is best characterized as being dominated by the ram pressure of the incident wind. In the intermediate case, such that $\mathcal{M}_\mathrm{w} \sim 0.1-1$, the flow still has a large amount of angular momentum, but the higher gas pressure allows the wind to thermalize and produce disk-like structures.

2.2. *Defining properties of the accretion flow*

It's worth taking a moment to contextualize our wind tunnel framework in the landscape of other accretion flows. Our setup is similar to other local simulations of accretion flows, which have proven effective tools for understanding both single and binary BH accretion in a variety of environments, including the ISM (Antoni et al. 2019; Kaaz et al. 2019, 2020, Schröder et al. 2021 in prep) and common envelope evolution (MacLeod & Ramirez-Ruiz 2015a,b; MacLeod et al. 2017; Murguia-Berthier et al. 2017; De et al. 2020; Everson et al. 2020). This family of accretion flows essentially considers permutations of Bondi-Hoyle-Lyttleton accretion (for a review, see Edgar 2004) characterized by the gas properties of the surrounding medium.

The case of the AGN disk is distinguished from these other scenarios by the large angular momentum content available to the embedded binary. In the limiting case of an effectively infinite angular momentum reservoir, one might expect accretion to resemble the commonly studied thin circumbinary disk ('CBD', Muñoz et al. 2019, 2020), where BBHs are expected to expand rather than contract due to positive gravitational torques from the surrounding gas. This is similar to the scenario explored by Baruteau et al. (2011) and more recently by Li et al. (2021), who performed global simulations of an AGN disk with an embedded binary system in two dimensions. In Li et al. (2021), they found that prograde embedded binaries also expand, as in the case of CBDs. We emphasize, however, that for these works to globally resolve the AGN disk and the binary, they are required to use large values of q and model the system in two dimensions. By using Equation 5, we can write $R_\mathrm{w}/H \approx 2q^{1/3}(H/R)^{-1} = 2\mathcal{M}_\mathrm{w}$. When q is large and H/R is small, $R_\mathrm{w} \gg H$, which justifies their two-dimensional approach. However, as we will find in the following section, for much of the $q-H/R$ parameter space, $H \gtrsim R_\mathrm{w}$ and the resulting flow is inherently three-dimensional, supported partially by rotation and partially by pressure gradients. This suggests a dichotomy in the geometry of accretion flows surrounding embedded binaries: in thin accretion disks hosted by lower mass ($\lesssim 10^6-10^7 M_\odot$)

SMBHs, the embedded binary may be better represented by the more traditional two-dimensional accretion flows studied by Baruteau et al. (2011) and Li et al. (2021). In either thicker AGN disks (i.e., for high Eddington ratios, or in the outer Toomre-stabilized regions discussed in the next section) or for more massive ($\gtrsim 10^7 M_\odot$) SMBHs, the embedded binaries may be better represented by the vertically stratified accretion flows studied here.

2.3. *Astrophysical context*

What value of $\mathcal{M}_\mathrm{w}$ appropriately represents the flow surrounding an embedded binary? We can answer this by applying our $\mathcal{M}_\mathrm{w}$ formalism to physical models of AGN disks. In particular, we consider Shakura-Sunyaev (S-S) (Shakura & Sunyaev 1973) and Sirko-Goodman (S-G) (Sirko & Goodman 2003) accretion disks. In the classical S-S disk, each disk annulus has Keplerian orbital energy that is gradually dissipated by some unspecified source of viscosity that is parameterized by the quantity α. While the S-S disk forms the basis for most modern disk models, it becomes gravitationally unstable at large distances (typically $\gtrsim 10^2-10^3$ SMBH gravitational radii). The S-G model addresses these issues by including an unspecified pressure term that forces the disk to be marginally Toomre stable where it would otherwise be unstable. In reality, the disk likely continuously forms stars in this outer region, and the stellar feedback from these populations holds the disk in its marginally stable state.

We can explore how $\mathcal{M}_\mathrm{w}$ depends on S-S and S-G AGN disk models by using Equation 7 to relate $\mathcal{M}_\mathrm{w}$ to the mass ratio q and disk aspect ratio H/R. The profile of $\mathcal{M}_\mathrm{w}$ can depend sensitively on the parameters of the AGN. For simplicity, unless said otherwise, we will assume the host AGN disk has the following parameters for the remainder of this work,

- A $10^8 M_\odot$ SMBH accretes at an Eddington ratio of $\lambda_\mathrm{Edd}^{(\mathrm{SMBH})} = 0.5$ with a radiative efficiency of $\eta = 0.1$

- Viscosity is proportional to the total (gas + radiation) pressure and $\alpha = 0.01$

- The embedded, equal-mass binary has a total mass $M = 60 M_\odot$

In the case of the S-G model, this is the same disk model used to study the orbital migration of embedded black holes in Secunda et al. (2019), who found that their migrating BHs became trapped at roughly $\approx 10^{-3}-10^{-2}$ pc.

In the left panel of Figure 2, we plot $\mathcal{M}_\mathrm{w}$ as a function of distance D in the AGN disk for both profiles. For the S-S profile, we show both a disk with H/R set by gas pressure (solid line) and by radiation pressure (dashed line) (Frank et al. 2002). We also shade two regions,
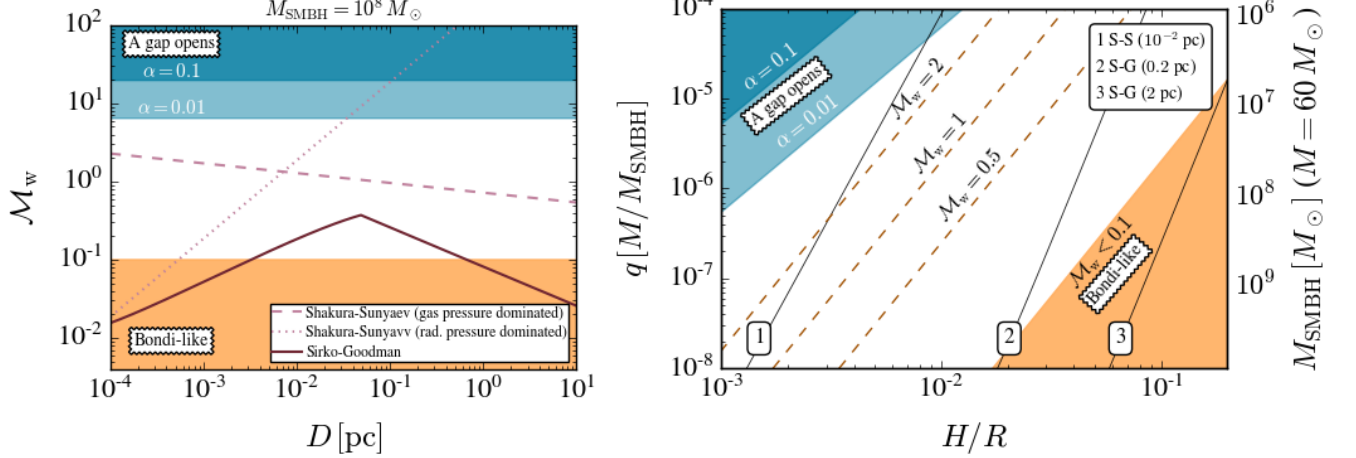
Figure 2. In both panels, we consider the dependence of $\mathcal{M}_w$ in Shakura-Sunyaev (S-S) and Sirko-Goodman (S-G) disk models. We assume an Eddington ratio of 0.5 and a viscosity parameter $\alpha = 0.01$. In the blue regions, we highlight where a gap is expected to open, given by the criterion in Equation 1 of Baruteau et al. (2011). The orange region shows when the accretion flow becomes Bondi-like (defined such that the analytic accretion rate is $\gtrsim 99\%$ of the Bondi rate). **Left panel.** Here, we plot $\mathcal{M}_w$ as a function of the BBH distance from the central AGN for different AGN disk models. **Right panel.** We show the mass ratio (q) - aspect ratio (H/R) plane, and depict $\mathcal{M}_w$ contours (Eq. 7) that correspond to our simulations. On the right vertical axis, we express q in terms of M_{SMBH}, given that $M = 60 M_\odot$. We also give examples of $q - H/R$ contours for different distances in both S-S and S-G models.

1. The lower orange region which we designate as 'Bondi-like' ($\mathcal{M}_w \lesssim 0.1$). Within this region, $\dot{M}$ (Eq. 12) deviates from the Bondi accretion rate (Bondi 1952) by only $\lesssim 1\%$. If this is the case, the velocity shear in the wind is mostly negligible, and the flow geometry is quasi-spherical.

2. The upper blue region where our binary opens a gap within the AGN disk. This is defined by the gap opening criterion provided in Equation 1 of Baruteau et al. (2011), and while it is insensitive to the specific disk profile it does depend on α.

We notice a few features immediately: first, it is unusual for $\mathcal{M}_w$ to exceed unity. An exception is the gas pressure dominated S-S curve, but only at small radii where the disk is in fact radiation pressure dominated at this value of $\lambda_{\mathrm{Edd}}^{(\mathrm{SMBH})}$. The radiation pressure dominated S-S curve has large $\mathcal{M}_w$ at large radii, but here the flow is gas pressure dominated. For the $S-G$ profile, which is more credible in the outer regions where the S-S disk is Toomre unstable, the flow is actually Bondi-like at regions beyond $\approx 1\,\mathrm{pc}$. We note the presence of the inflection point at $\approx 0.05\,\mathrm{pc}$ in the S-G profile, which marks the transition between the inner disk and the Toomre-stabilized outer disk (see for reference Fig. 2 of Sirko & Goodman 2003, which depicts the same profiles used here).

In the right panel of Figure 2, we plot contours of $\mathcal{M}_w$ in the $q - H/R$ plane (Eq. 7), and shade the same 'Bondi-like' (orange) and 'gap-opening' (blue) regions as in the left panel. The vertical axis in this panel is alternatively labeled in terms of M_{SMBH}, given $M = 60 M_\odot$. We have labeled $\mathcal{M}_w = 0.5, 1$

and 2 isocontours, which correspond to the hydrodynamic simulations that we present in Section 3. The gap opening criterion is satisfied only for particularly thin accretion disks with particularly high mass ratios. This point deserves emphasis, as there are conflicting claims in the literature regarding gap formation in AGN disks. In Baruteau et al. (2011), gap formation happens primarily because they use an unrealistically small value of $\alpha = 8 \times 10^{-4}$ ($\alpha \approx 0.01 - 0.3$ is more realistic for AGN disks, e.g. King et al. 2007), and gap opening is clearly sensitive to this parameter as can be seen in Fig. 2. In Bartos et al. (2017), they also invoke gap opening, but use a disk model that is thinner than both S-G and S-S models, causing $\mathcal{M}_w$ to be larger. In Stone et al. (2017), they also find that gaps are unlikely to open anywhere in the disk, and they use the AGN disk model from Thompson et al. (2005). This model is comparable to the S-G model because they also construct profiles that are marginally Toomre stable in the outer regions. All embedded BBHs that form in situ will, by definition, be born in these outer regions, and many dynamically captured embedded BBHs will be captured at larger radii, so we favor disk models that account for this region. Still, it is clear that different disk models can yield different results, and more work needs to be done so the community can come to consensus on which disk model is most favorable.

3. HYDRODYNAMICS

3.1. *Simulations*

To test our $\mathcal{M}_w$ formalism, we performed three-dimensional hydrodynamic simulations of accretion onto embedded

BBHs using version 4.5 of the grid-based, adaptive mesh refinement hydrodynamics code FLASH (Fryxell et al. 2000). We use a local, wind tunnel computational domain that is continuously replenished with a shearing gaseous wind (see the arrows in the inset panels of Fig. 1). Physically, the velocity profile of the wind is the Keplerian velocity about the SMBH, in the rest frame of the BBH, which we approximate using the linearized velocity profile defined in Equation 4. For simplicity, we neglect gradients in the gas density and sound speed of the wind, setting them to ambient values ρ_∞ and c_∞ respectively. We evolve our simulations in a scale-free fashion, where $c_\infty = R_b = 1$ and $\rho_\infty = 10$. We relate the linearized velocity profile in Equation 4 to our scale-free setup by rewriting it as,

$$v(y) = y \frac{c_\infty \mathcal{M}_w^3}{2R_b} \tag{8}$$

where we have substituted δr for y.

When constructing the domain, we neglect vertical gradients in the wind, acknowledging that when $\mathcal{M}_w > 1$ the AGN disk scale height H becomes comparable to the BBH sphere of influence which should be considered in future studies. We also neglect centrifugal and coriolis accelerations from the SMBH potential. The width of our computational domain is $32R_b$ in each Cartesian direction, with the wind oriented in the $\pm \hat{x}$ direction and generated every timestep at the x boundaries of the domain. For the y and z directions, we use outflow boundary conditions.

We evolve the BBHs using the active sink particles module that was developed for FLASH by Federrath et al. (2010), and use the same implementation of it as Antoni et al. (2019). While we refer the reader to these works for complete descriptions of our sink prescription, the most salient details are as follows. The binary is initialized with its center of mass at $x = y = z = 0$ and occupies a circular orbit with semimajor axis a in the the $x - y$ plane. The $+z$ axis is parallel to the angular momentum vectors of the binary orbit and the AGN disk. We model the BBHs using Newtonian gravitational potentials with an absorbing boundary condition centered at the location of each binary companion. These absorbing boundaries have sink radii $R_s = 0.0125R_b$, and any gas that crosses this boundary is removed from the domain, with the mass and angular momentum of the removed gas being recorded and added to the corresponding binary member. We also check the convergence of our mass accretion and inspiral rates with sink radius in Section A. While the rate of inspiral is converged, the mass accretion rate decreases with decreasing sink radius. The non-convergence of the mass accretion rate with sink radius is a known issue with the sink prescription in Bondi-like accretion flows (Xu & Stone 2019; De et al. 2020) and so the accretion rates derived from these simulations should be taken as upper limits. We adaptively

refined around the region closest to the binary members, with smallest cell size $\delta r_{min} \approx 0.0039R_b$. This means that there are $R_s / \delta r_{min} = 3.2$ cells across a sink radius, a value that was tested for convergence in Antoni et al. (2019).

In total, we present six simulations, varying $\mathcal{M}_w$ and a/R_b, where a is the BBH semimajor axis. We use values $\mathcal{M}_w = 0.5$, 1, and 2, and $a/R_b = 0.1$ and 1. We use a gamma-law equation of state, and assuming that the gas in the AGN disk can cool efficiently, take $\gamma = 1.1$ [1]. In each simulation, the BBH occupies a circular, equatorial orbit that is prograde with the angular momentum of the wind. Each simulation was run until $t = 50R_b/c_\infty$, well into steady state as shown in Appendix A. In the following two subsections, we present the results of these simulations.

3.2. *Flow*

In Figure 3, we show the large-scale flow morphology of each simulation. In the top, 2×3 panel subfigure, we depict $12 \times 12R_b$ equatorial slices of the gas density. When $\mathcal{M}_w = 0.5$, the flow is structured and laminar, with an extended density profile that is wound in a direction prograde with the binary angular momentum. When $\mathcal{M}_w = 2$, the flow becomes 'unwound', with tails that follow the direction of the wind. Additionally, the flow is characterized by a clumpy, turbulent density distribution and by large-scale shocks that trail from the BBH. When $\mathcal{M}_w = 1$, the flow shares characteristics of both the $\mathcal{M}_w = 0.5$ and 2 simulations. It is evident from these 2D slices that there is some degree of rotational support to the flow, which can be quantified with the circularization radius of the wind,

$$R_{circ} = \frac{GM}{v^2(y = R_{circ})} \rightarrow R_{circ} = \mathcal{M}_w^{-2} 4^{1/3} R_b \tag{9}$$

For $\mathcal{M}_w = 0.5$, 1 and 2, the corresponding circularization radii are $R_{circ} \approx 6.4$, 1.6 and $0.4R_b$. These values roughly correspond to the extent of the density structures in each simulation, particularly when $a/R_b = 0.1$.

The main difference between the $a/R_b = 0.1$ and 1 simulations is that in the former, the accretion flow forms a high-density envelope shared by both binary companions, while in the latter each companion has its own envelope. This makes sense, because when $a/R_b = 0.1$, the semimajor axis of the binary is much smaller than the sphere of influence, while when $a/R_b = 1$, they are comparable.

In the bottom, 1×3 panel subfigure of Figure 3, we show 3D gas density contours from each $a/R_b = 1$ simulation. As also seen in the 2D subfigure, when $a/R_b = 1$ each binary companion has its own high-density envelope, which overlap more when $\mathcal{M}_w$ is smaller. As $\mathcal{M}_w$ increases, the peak

---

[1] In cases where the accretion rate is super-Eddington, the flow is radiation dominated and $\gamma = 4/3$ would be more appropriate, but we leave the explicit effects of radiation to be considered in a later work.
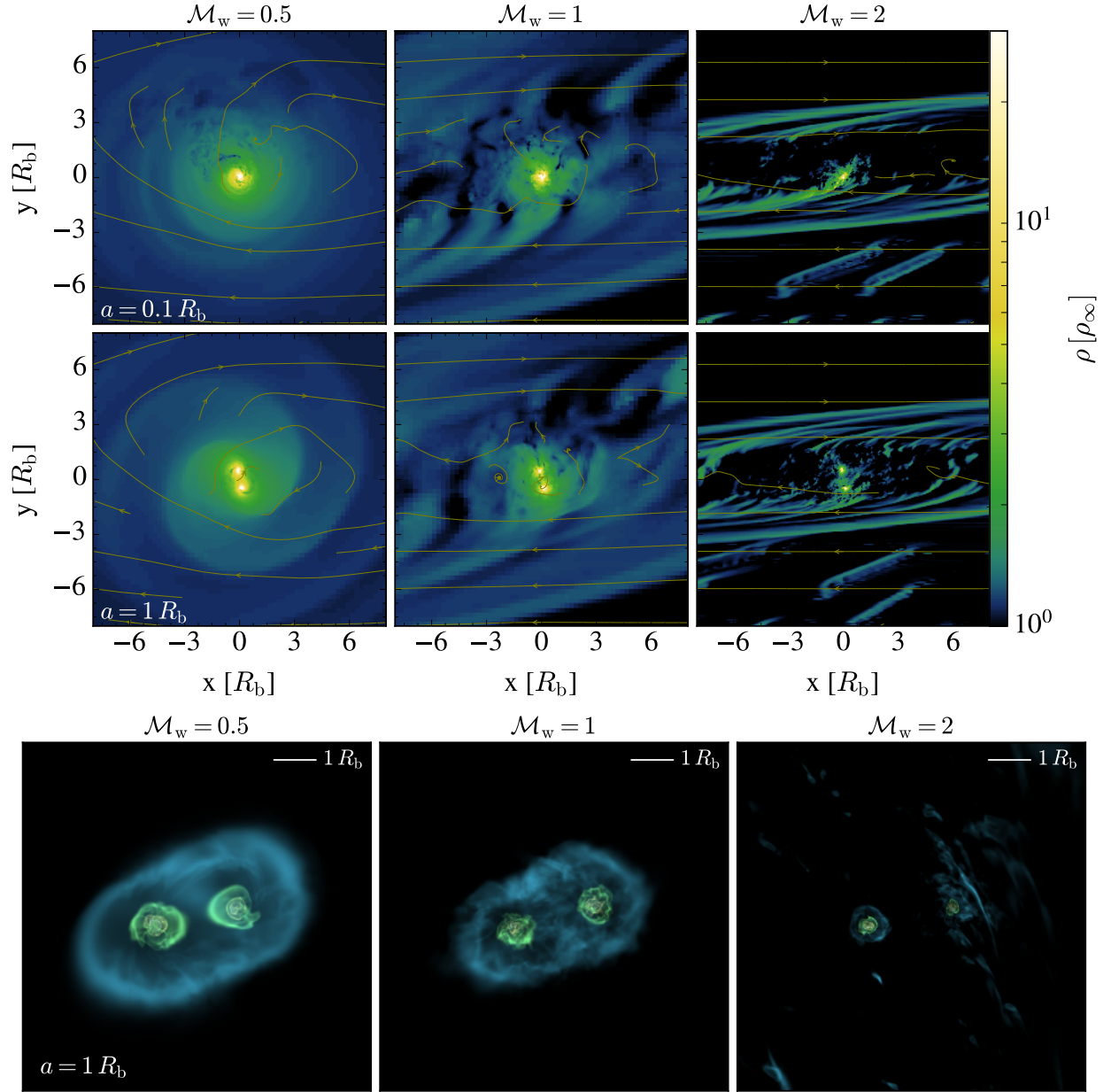
Figure 3. Upper panel. Here, we highlight the large scale flow morphology for each of our simulations by plotting $12 \times 12\,R_{\rm b}$ slices of gas density at late times. Each column from left to right represents increasing local Mach number $\mathcal{M}_{\rm w}$, where at high $\mathcal{M}_{\rm w}$ the ram pressure of the wind prevents stable flow structures from forming. In each row, we plot different values of the binary semimajor axis a. At small a, the binary shares a density enhancement, whereas at large a each binary member has its own density enhancement. **Lower panel.** We plot 3D gas density isocontours for each of our $a = 1\,R_{\rm b}$ simulations at the same times as the upper panel. As $\mathcal{M}_{\rm w}$ increases, the density enhancements surrounding each BH become smaller.

density remains similar, but each density envelope becomes truncated. While in the 2D subfigure the flow appears disk-like, we see from the 3D panel that the density envelopes are as extended in the vertical directions as they are in the equatorial directions. This suggests that the flow structures surrounding embedded BBHs are partially Bondi-like, and partially disk-like.

3.3. *Accretion & Inspiral*

The orbits of our simulated BBHs evolve due to a combination of gas drag and the accretion of mass and angular momentum. To compare to our numerical results, we will begin by writing down the analytic binary inspiral rate, $\dot{a}/a$. The full expression for $\dot{a}/a$, with the noted absence of gravitational-wave decay, is

$$\frac{\dot{a}}{a} = \frac{2\dot{L}}{L} - \frac{\dot{M}}{M} + \left(\frac{\dot{a}}{a}\right)_{\rm drag} \tag{10}$$

where the first two terms follow from assuming that the specific angular momentum of the binary is Keplerian $\left(\ell = \sqrt{GMa}\right)$. The third term represents an estimate for the gas drag contribution to the binary evolution, and is found to always be negative in our work. This is in contrast to hydrodynamic simulations of thin, gap-forming circumbinary disks where the drag term is found to be positive, e.g. Muñoz et al. (2019). To determine $\dot{L}$ and $\dot{M}$, we integrate over streamlines entering the gravitational sphere of influence of the BBH. We start by defining the length-scale,

$$R_{\mathrm{bw}} = \frac{R_{\mathrm{b}}}{1 + \frac{1}{2}\mathcal{M}_{\mathrm{w}}^2} \qquad (11)$$

which smoothly transitions between R_{b} when $\mathcal{M}_{\mathrm{w}} \ll 1$ and R_{w} when $\mathcal{M}_{\mathrm{w}} \gg 1$. This allows us to smoothly characterize the sphere of influence of the BBH across flow regimes analytically. The integral for the mass accretion rate is,

$$\dot{M} = \rho_\infty \int_{r < R_{\mathrm{bw}}} v(y) dA$$
$$= 4\pi R_{\mathrm{bw}}^2 \rho_\infty c_\infty \left(\frac{\mathcal{M}_{\mathrm{w}}^3}{8 + 4\mathcal{M}_{\mathrm{w}}^2} + 1 \right), \qquad (12)$$

and the integral for the angular momentum accretion rate is,

$$\dot{L} = \rho_\infty \int_{r < R_{\mathrm{bw}}} v^2(y) y dA$$
$$= \frac{\pi}{6} \rho_\infty c_\infty^2 \mathcal{M}_{\mathrm{w}}^6 R_{\mathrm{bw}}^3 \left(1 + \frac{1}{2}\mathcal{M}_{\mathrm{w}}^2 \right)^{-2}. \qquad (13)$$

These calculations assume that *all* streamlines entering the BBH sphere of influence are accreted, though in reality some fraction of this material is advected away due to gas and ram pressure, so Equations 12 and 13 should be considered upper limits. To estimate $\left(\frac{\dot{a}}{a}\right)_{\mathrm{drag}}$, we follow the approach of Antoni et al. (2019), who determined the inspiral rate for a BBH embedded in a Bondi-Hoyle wind tunnel (e.g., Edgar 2004; Blondin & Raymer 2012),

$$\left(\frac{\dot{a}}{a}\right)_{\mathrm{drag}} = 8\sqrt{2}\pi\lambda_s(\gamma)\rho_\infty c_\infty^{-3} G^2 M \left(1 + 4\frac{a}{R_{\mathrm{b}}} \right)^{-1/2} \qquad (14)$$

This calculation assumes that the orbital energy of the binary is dissipated by a gravitational wake induced by each component of the binary as they orbit through a dense gaseous envelope and assumes that the density of this envelope is given by the Bondi density profile evaluated at $r = a$, which is $\rho = \rho_\infty \lambda_s(\gamma)(a/R_{\mathrm{b}})^{-3/2}$, where we use $\lambda_s(\gamma = 1.1) \approx 1$ (Shapiro & Teukolsky 1983). We emphasize that the unperturbed background medium has zero net angular momentum in the case of Bondi and Bondi-Hoyle accretion, which contrasts with our flow geometry. Still, we expect this drag calculation to remain useful as a coarse estimate, particularly
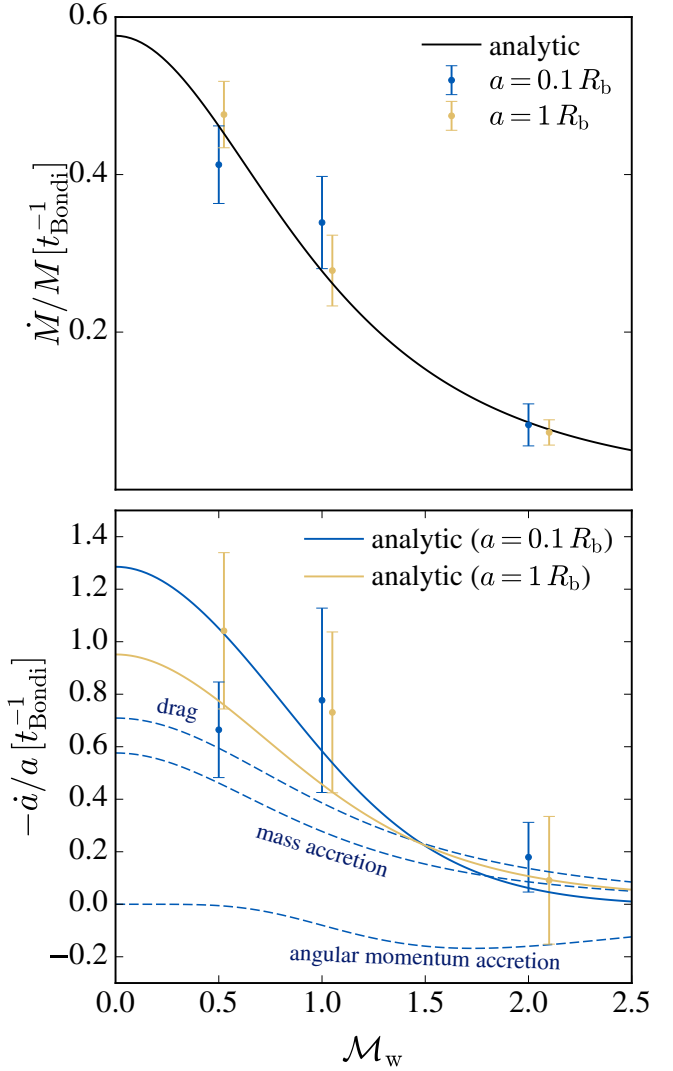
Figure 4. We compare our simulated accretion (top panel) and inspiral (bottom panel) rates to our analytic estimates (Equations 10-14) as a function of $\mathcal{M}_{\mathrm{w}}$. Both quantities are expressed in units of t_{Bondi}^{-1}, which is the Bondi accretion rate per unit mass, given by Equation 12 as $\mathcal{M}_{\mathrm{w}} \to 0$. For the $a = 0.1\,R_{\mathrm{b}}$ simulations, we also show the various contributions to $\dot{a}$ (drag, mass accretion, angular momentum accretion) with dashed lines. As $\mathcal{M}_{\mathrm{w}} \to 0$, both profiles approach a Bondi solution. Care should be taken in extrapolating to $\mathcal{M}_{\mathrm{w}} \gg 1$, as at high values $R_{\mathrm{w}} \gg H$ and the flow geometry is two-dimensional, making our wind tunnel simulations less appropriate (see Baruteau et al. 2011, for comparison).

when $\mathcal{M}_{\mathrm{w}}$ is small and the flow becomes more Bondi-like (e.g., Fig. 1).

In Figure 4, we assess how well our analytic estimates compare to our simulated values for the accretion and inspiral rates as a function of $\mathcal{M}_{\mathrm{w}}$. We express our rates in units of $t_{\mathrm{Bondi}}^{-1} = \dot{M}_{\mathrm{Bondi}}/M$, which is the Bondi accretion rate per unit mass (Bondi 1952) and is given by Equation 12 as $\mathcal{M}_{\mathrm{w}} \to 0$. We scale our analytic mass accretion (Eq. 12) and drag (Eq. 14) rates to constant numerical prefactors, 0.576

for $\dot{M}$ and 0.298 for $\left(\frac{\dot{a}}{a}\right)_{\mathrm{drag}}$. Using these adjustments, Fig. 4 shows that our analytic estimates reasonably reproduce our simulated result. In general, the binaries accrete and inspiral on similar timescales, with inspiral occurring slightly faster. This is in contrast to what is seen in Bondi-Hoyle accretion onto binaries, e.g. Fig. 11 of Antoni et al. (2019), where inspiral happens about $3-4$ times faster than accretion. While a factor of $3-4$ difference seems small, it can change the final mass of the binary at the time of merger significantly. This is because the mass growth has an exponential dependence on this factor, which we will discuss further in Section 4.2. We note that when $\mathcal{M}_{\mathrm{w}} \gg 1$, our local wind tunnel approximation breaks down because the BBH can begin influencing the AGN disk, so care should be taken in extrapolating to larger values of $\mathcal{M}_{\mathrm{w}}$. In those cases, the flow geometry is likely better represented by the results of Baruteau et al. (2011). In contrast, extrapolating our mass accretion prescription to $\mathcal{M}_{\mathrm{w}} = 0$ provides no issue, as the flow approaches a Bondi solution in that limit. We do note that the inspiral rate in our $\mathcal{M}_{\mathrm{w}} = 0.5$ simulation deviates from our fit; it is possible that as the flow becomes more Bondi-like, the resulting symmetry causes the partial cancellation of gravitational torques from the gas. Still, this is only an order unity deviation, and does not appreciably affect the application of our results in the following sections.

While for completeness we included the $\dot{L}$ term in Equation 10, we see from Fig. 4 that it weakly contributes to the inspiral. Additionally, we follow the accretion flow down to some prescribed sink radius R_{s} (described in Section 3.1 and Appendix A), which is much larger than the event horizons of the black holes. In real systems, most positive angular momentum has to be transported radially outwards if the binary is to accrete. This likely makes $\dot{L}$ negligible, which we discuss further in Subsection 4.2.

4. EVOLUTION OF EMBEDDED BBHS

4.1. *How does the binary first become embedded?*

To determine the evolution of embedded BBHs, it is important to understand how they are first captured. The BBH is either born in the outer regions of the disk or, having previously existed in the nuclear cluster when the disk was formed, it gradually aligns with the disk. The initial position of the embedded BBH is determined by how it became embedded, which strongly impacts the binary's subsequent evolution.

Roughly $\approx 80\%$ of stars in the nuclear cluster are expected to have formed in situ (Antonini et al. 2015). If the BBH is formed directly in the disk (as studied in Stone et al. 2017), it by definition will start in the Toomre-stabilized region as this is where star formation occurs. In Fig. 5 of Thompson et al. (2005), they generally find that the star formation rate (SFR) in nuclear starburst disks increases as a function of radius. This would suggest that the vast majority of embedded BBHs

formed in situ will begin their journeys at large ($\gtrsim 1-10\,\mathrm{pc}$) radii in the AGN disk. The possibility that they merge in the inner regions of the AGN disk depends on the relative efficiency of inspiral versus migration.

The dynamical capture of BBHs by AGN disks depends on the distribution of stellar-mass BHs (sBHs) in the nuclear cluster (NC). This distribution is often chosen by invoking the inferred distribution of the black hole cusp surrounding Sag A*, which roughly scales as $\propto D^{-2.5}$ (Bartko et al. 2009; Alexander & Hopman 2009) and likely has ~ 1000 sBHs in the inner $0.1\,\mathrm{pc}$ (Antonini 2014; Hailey et al. 2018). However, the formation of this cusp requires that the stellar population has relaxed around the central SMBH (Bahcall & Wolf 1976). The relaxation timescale for a $10^6\,M_{\odot}$ SMBH can range from $0.1-10\,\mathrm{Gyr}$ (O'Leary et al. 2009), and can exceed a Hubble time for more massive SMBHs. So, it may be that heavier SMBHs harbor no black hole cusp during the AGN phase, which makes the viability of the dynamical capture channel less certain. For this reason, we favor the in situ formation of embedded BBHs, which should begin their journey in the AGN disk at larger ($\gtrsim 1\,\mathrm{pc}$) distances.

4.2. *Binary Evolution*

Once BBHs become embedded in the AGN disk, they will simultaneously inspiral, migrate and grow in mass. In this section, we model these processes by evolving a system of coupled ordinary differential equations for $\dot{D}$ (migration), $\dot{M}$ (accretion), and $\dot{a}$ (inspiral). To guide our intuition, we begin by estimating the timescales associated with each of these processes, as depicted in Figure 5. We use an S-G AGN disk model with $M_{\mathrm{SMBH}} = 10^8$, $\alpha = 0.01$, $\lambda_{\mathrm{Edd}}^{(\mathrm{SMBH})} = 0.5$ and assume that the viscosity is proportional to the total (gas + radiation) pressure. At a characteristic distance of $1\,\mathrm{pc}$ for a $60\,M_{\odot}$ binary, the migration timescale is

$$
\begin{aligned}
t_{\mathrm{migr}} \approx 279\,\mathrm{Myr} & \left(\frac{H/R}{10^{-1}}\right)^2 \left(\frac{q_d}{0.14}\right)^{-1} \left(\frac{M}{60\,M_{\odot}}\right)^{-1} \\
& \times \left(\frac{M_{\mathrm{SMBH}}}{10^8\,M_{\odot}}\right)^{1/2} \left(\frac{D}{1\,\mathrm{pc}}\right)^{3/2},
\end{aligned}
\tag{15}
$$

which we acquire from Equation 10 of Paardekooper (2014). Here, q_d is the ratio of the enclosed disk mass to M_{SMBH} at a distance D in the AGN disk. This characteristic timescale is long compared to the lifetime of the disk ($\approx 50-150\,\mathrm{Myr}$), but can become as short as $\approx 3\,\mathrm{Myr}$ at $D \approx 0.05\,\mathrm{pc}$ (blue-green line in Fig. 5).

At large semimajor axes, before gravitational-wave emission dominates, binaries inspiral due to the combined influence of mass accretion and drag. At distances of $\gtrsim 0.5\,\mathrm{pc}$, the accretion flow is Bondi-like (e.g., Fig. 2), for which the
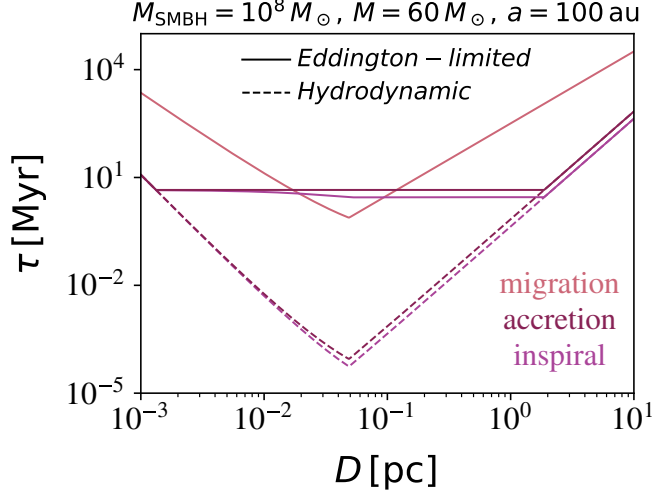
Figure 5. We plot characteristic timescales associated with the migration, mass accretion and inspiral of an embedded BBH as a function of distance in the AGN disk. Here, we consider the case of a $60 M_\odot$ binary with semimajor axis $a = 100$ au that is embedded in an AGN with host mass $M_{\rm SMBH} = 10^8 M_\odot$ accreting at an Eddington ratio $\lambda_{\rm Edd}^{\rm (SMBH)} = 0.5$. The hydrodynamic accretion and inspiral rates (dashed lines) follow from Equations 12 and 10, respectively. At most locations in the disk, the mass accretion rate is Eddington-limited, which will also limit the efficiency of drag and thus the inspiral rate (solid lines). In the solid inspiral curve, we assume that drag is proportionate to the accretion rate and thus Eddington-limited whenever the accretion rate is, though as discussed in Section 4.2 this likely places a lower limit on the efficiency of drag.

mass doubling time ($\equiv M/\dot{M}_{\rm Bondi}$) is characteristically

$$t_{\rm Bondi} \approx 74\,{\rm Myr} \left(\frac{M}{60 M_\odot} \right)^{-1} \left(\frac{\rho}{10^{-18}\,{\rm g\,cm}^{-1}} \right) \left(\frac{c_s}{25\,{\rm km\,s}^{-1}} \right)^{-3} \tag{16}$$

The associated drag timescale ($\equiv$ the inverse of Eq. 14) is characteristically

$$t_{\rm drag} \approx 26\,{\rm Myr} \left(\frac{\rho}{10^{-18}\,{\rm g\,cm}^{-3}} \right) \left(\frac{c_s}{25\,{\rm km/s}} \right)^{-3} \left(\frac{M}{60 M_\odot} \right) \tag{17}$$

Since the timescale for drag is shorter than that for accretion, it more dominantly contributes to the inspiral. The accretion and inspiral timescales are depicted by the dashed lines in Fig. 5. We immediately see that the inspiral rate essentially follows the mass accretion rate, which is because it depends most strongly on the density of gas enveloping the binary. The two trajectories aren't exactly parallel, but this is primarily due to the nonlinear dependence on $\mathcal{M}_{\rm w}$ in Equations 12 and 14. We also see that the migration timescale is always much longer than the hydrodynamic inspiral and accretion timescales, which at first would suggest the binaries essentially evolve in place without migrating. However, through the majority of the disk's extent, the mass accretion rate is super-Eddington and a purely hydrodynamic approach is likely too simplified. The nature of super-Eddington ac-

cretion flows, especially around binaries, remains unclear, so we take the simplest approach and limit mass accretion to the Eddington limit,

$$\dot{M}_{\rm Edd} = \frac{L_{\rm Edd}}{\eta c^2} \tag{18}$$

Simulations of super-Eddington accretion have shown that mass accretion rates can significantly exceed the Eddington rate (McKinney et al. 2014, 2015; Dai et al. 2018), which is essentially set by how small the radiative efficiency (η) is. Thin disks have typical values of $\eta = 0.1$, which lowers to roughly $\eta = 0.01$ near the Eddington limit, and can be even smaller at significantly super-Eddington rates. For simplicity, we adopt a constant value of $\eta = 0.01$. The associated Eddington accretion timescale ($\equiv M/\dot{M}_{\rm Edd}$) is independent of mass,

$$t_{\rm Edd} \approx 4.5\,{\rm Myr} \left(\frac{\eta}{0.01} \right) \tag{19}$$

We must make a few modifications for the inspiral rate in our binary evolution prescriptions. First, we include a term for the gravitational wave inspiral rate of an equal-mass binary (Peters 1964). Second, we neglect the $\dot{L}$ term in Eq. 10, since our hydrodynamic simulations demonstrate that this term only weakly contributes to the binary's evolution (Fig. 4). The sink radii we prescribe are also much larger than the event horizon. In real systems, the majority of angular momenta must be either viscously or mechanically transported outwards for material to be accreted, making $\dot{L}$ negligible.

What is less clear is how drag changes when accretion is Eddington-limited. If most material fed to the BBH is ejected by super-Eddington outflows, the diminished gas density should make drag less efficient. However, drag occurs due to the gravitational influence of all material inside the BBH sphere of influence. If material is only ejected near the innermost stable orbits (ISCOs) of the companion BHs, drag may only be marginally affected by outflows. We proceed by comparing two different prescriptions for drag in the super-Eddington regime.

In the first prescription, we assume that outflows evacuate gas uniformly from the entire sphere of influence, which causes the drag rate to be $\propto \dot{M}$. So, when the mass accretion rate is Eddington-limited, so is the drag rate. In reality, outflows operate more strongly near the ISCOs of the BHs, and there may actually be very little evacuation of gas within most of the BBH sphere of influences. For instance, if outflows only weakly affect the gas density at the semimajor axis, drag may only be marginally inhibited. In consequence, this prescription likely underestimates drag because it underestimates the gas density in the black hole sphere of influence. Because this makes the time-to-merger longer, the BBHs can grow more significantly in mass under this assumption.

In the second prescription, we limit drag based on more careful assumptions. First, we assume that drag depends

linearly on the gas density at the semi-major axis, which is the case for the hydrodynamic drag rate (Equation 14). The gas density is proportionate to the mass accretion rate, $\dot{M}$, which in the case of pure inflow would be constant. However, for super-Eddington flow $\dot{M}$ decreases closer to the IS-COs of the black holes due to the loss of material by winds. We assume that mass loss due to winds occurs down to the photon-trapping radius, r_{pt}, which we define following King & Begelman (1999),

$$r_{pt} = \frac{\dot{M}}{\dot{M}_{Edd}} r_s, \tag{20}$$

where r_s is the Schwarzschild radius. At $r < r_{pt}$, photons are accreted faster than they can diffuse out of the flow, inhibiting radiation-driven outflows. So, at large radii, the mass accretion rate is unchanged from its hydrodynamic value (Eq. 12), and decays to $\dot{M}_{Edd}$ at $r = r_{pt}$. We assume that for $r_{pt} < r < R_{bw}$, that the accretion rate depends linearly on radius. So, when $r_{pt} > a$, all winds are ejected at large radii and the drag rate is $\propto \dot{M}_{Edd}$. When $r_{pt} < a$, the drag rate is $\propto \dot{M}_{Edd} \frac{a}{r_{pt}}$ (as long as this factor doesn't exceed the hydrodynamic mass accretion rate). The consequence of using this prescription is that mass accretion is limited more significantly than drag, causing inspiral to happen faster relative to mass accretion.

We evolve our binaries in Figure 6, where we show how the binary separation, mass, and AGN disk position change in time. In the left panel, we use our first super-Eddington drag prescription where we Eddington-limit the drag rate, and in the second panel we use the second super-Eddington drag prescription that depends on the photon trapping radius. We initialize our evolved binaries with semi-major axes $a = 100$ au, masses $M = m_1 + m_2 = 20$ and $60 M_\odot$, and initial distances $D = 0.1$, 1, and 2 pc. We use $\lambda_{Edd}^{(SMBH)} = 0.5$ on the left subfigure of both panels and $\lambda_{Edd}^{(SMBH)} = 0.05$ on the right. Each integration is terminated when the semimajor axis reaches $a = 0.1$ au, after which the inspiral becomes rapid due to gravitational-wave decay. In all cases, the full evolution occurs on timescales of $\approx 5 - 30$ Myr. The relative hierarchy of timescales is as follows; the binary inspirals the quickest, and is driven to inspiral by a combination of drag, gravitational-wave radiation, and mass accretion. Second, the masses begins to increase, and in some cases double. For the Eddington-limited drag prescription, this occurs nearly as quickly as inspiral, causing the binary masses to grow to hundreds of solar masses. For the photon trapping drag prescription, this occurs more slowly than inspiral, reducing how high the BH masses are at the time of merger. At distances $\gtrsim 1$ pc, migration is negligible; however, at $D \lesssim 0.1 - 1$ pc, migration can occur at a comparable rate to mass accretion and inspiral.

How much should we trust the mass growth rates presented in Figure 6? We can answer this by estimating how sensitive our final BH masses are to uncertainties in the inspiral and mass accretion rates. If the time-to-merger is set by some inspiral timescale, $\tau_{inspiral}$, then the ratio $\tau_{inspiral}/\tau_{accretion}$, where $\tau_{accretion}$ is the accretion timescale, will dictate the final mass of the BBH at the time of merger. If we assume these timescales are constant, then $a(t) = a_0 \exp(-t/\tau_{inspiral})$ and $M(t) = M_0 \exp(t/\tau_{accretion})$. Since the initial semi-major axes of our binaries are $a_0 = 100$ au and we end our evolutionary tracks when they reach $a = 0.1$ au, then $t_{merger} \approx 7 \tau_{inspiral}$. We can then rewrite our expression for mass growth as $M(t = t_{merger}) = M_0(a_0/a)^{\tau_{inspiral}/\tau_{accretion}} = M_0(10^3)^{\tau_{inspiral}/\tau_{accretion}}$. This lets us see that the final binary masses are highly sensitive to the ratio $\tau_{inspiral}/\tau_{accretion}$, and an order-unity change in this ratio can result in an order-of-magnitude difference in the final binary mass. Since there are clear systematic uncertainties in our assumptions - such as the efficiency of drag in the super-Eddington regime - there must certainly be errors in our prescribed mass accretion and drag rates that are at least order-unity. As such, Figure 6 can only provide broad insights about the mass growth of embedded BBhs, and the final mass could be anywhere between $\lesssim 2$ to $\approx 10^2$ times the initial mass. In the future, it will require a better understanding of super-Eddington binary accretion to more precisely predict the final masses of embedded BBHs at the time of merger.

In general, the evolution of the binary happens well within the lifetime of the AGN disk ($\approx 50 - 150$ Myr, labeled τ_{AGN} in Fig. 6). However, a potentially important caveat in this evolution is that we keep the AGN disk static. In reality, the AGN disk can 'flicker' on short timescales ($\approx 0.1 - 10$ Myr, labeled $\delta\tau_{AGN}$ in Fig. 6) (e.g., Schawinski et al. 2015). Similar phenomena is seen in the simulations of Angles-Alcazar et al. (2020), who found that the gas supplying luminous quasars can restructure and change orientation on timescales of $\approx 0.1 - 1$ Myr. If the binary becomes embedded, but then within $\delta\tau_{AGN}$ the disk restructures and reorients itself, the BBH may once again require its inclination to be damped with respect to the restructured disk for a gas-assisted inspiral to proceed.

5. DISCUSSION

5.1. *Implications for gravitational-wave signals*

The results of Figure 6 have profound implications for the gravitational-wave signals observed by LIGO and Virgo. If a BBH becomes embedded within an AGN disk, it can be driven to merger on timescales $\lesssim 5 - 30$ Myr. While the rates at which BBHs form within AGN disks is unclear, our calculations suggest that gas-assisted inspiral is a viable formation channel for BBH merger events. Furthermore, the BHs in these binaries accrete at significant rates, suggesting that a
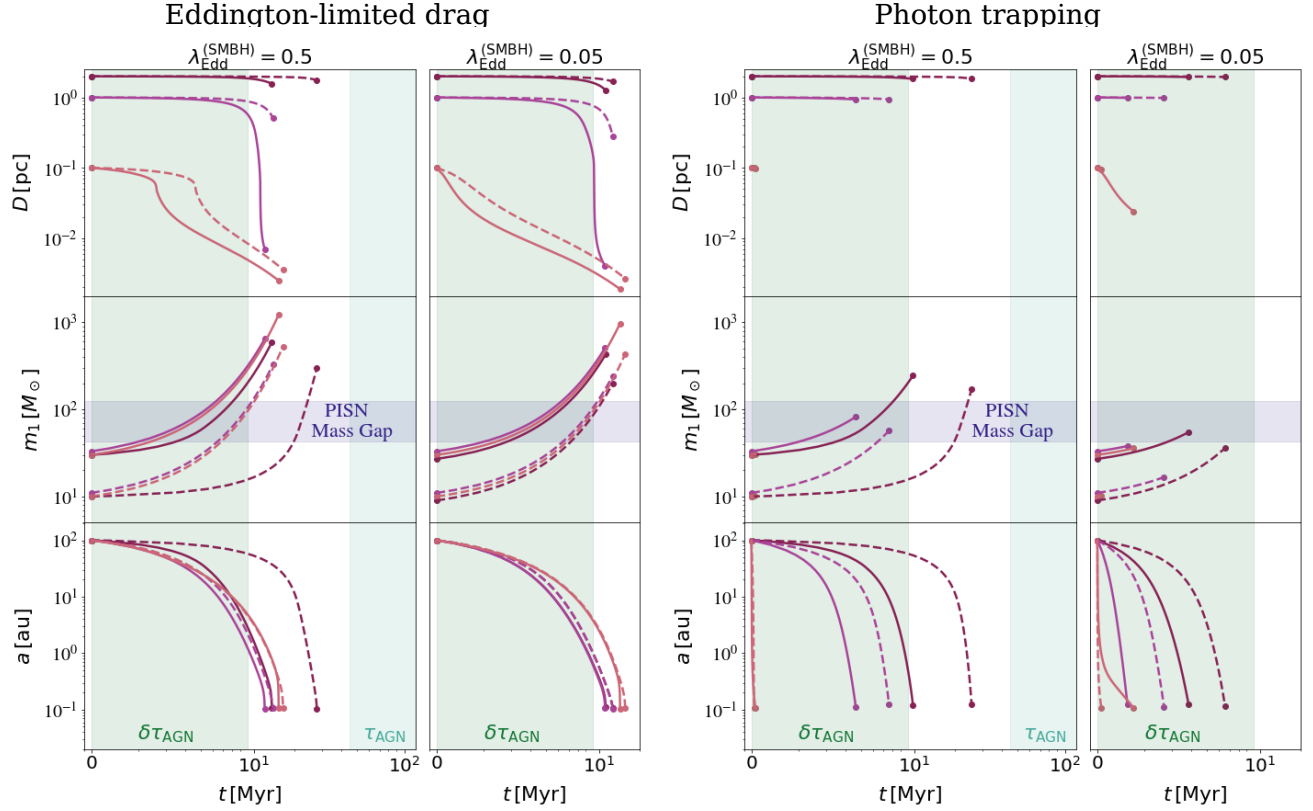
Figure 6. We plot the integrated evolution of binaries embedded in an AGN disk with initial separations of $a = 100$ au, initial distances from the SMBH $D = [0.1, 1, 2]$ pc and initial masses $M = m_1 + m_2 = 20$ and $60 M_\odot$. We specifically consider migration within the AGN disk, mass growth, and inspiral rate. We do this for Sirko-Goodman disk models for Eddington ratios of 0.5 and 0.05, where we take $M_{SMBH} = 10^8$, $\alpha = 0.01$, and assume that viscosity is proportional to the total (gas+radiation) pressure. We shade regions based on the typical duty cycle of an AGN, τ_{AGN}, and on the timescale on which AGN disks flicker and restructure themselves, $\delta\tau_{AGN}$. Shaded in purple is the mass range associated with the pair instability supernova mass gap. In the left panel, we assume that drag is Eddington-limited whenever the mass accretion rate is. In the right panel, we assume that drag lies between its hydrodynamic and Eddington-limited values, and depends on the ratio of semi-major axis to photon trapping radius (see Section 4.2 for a more detailed description).

pair of $30 + 30 M_\odot$ BHs can potentially evolve into the pair instability supernova mass gap. Such a system was recently observed by LIGO/Virgo (Abbott et al. 2020; Abbott et al. 2020), with a reported possible association with an electromagnetic transient event in an AGN (Graham et al. 2020). If further analysis confirms the association or if additional associations are identified with future LIGO events, such signals would amount to a confirmation of the merger channel studied here.

A caveat is that the accreting BHs in our paradigm should significantly spin up and become aligned, leading to a large effective spin parameter, $\chi_{eff} \gtrsim 0.9$. In contrast, the GW190521 gravitational wave signal was associated with a much smaller value of $\chi_{eff} = 0.08$. This suggests that the BHs either had low spins individually or had large spins that were misaligned with the orbit. If GW190521 did come from the AGN disk formation channel, then there must be some difference in the evolutionary process that we characterized in Section 4.2. A few plausible scenarios are,

1. While we focus on embedded BBHs, individual BHs will migrate and accrete mass from the disk in an analogous way. The inner parsec surrounding the host SMBH may be replete with these single BHs, each of which can potentially grow to sufficiently large masses that they enter the PISN mass gap. These BHs could then pair and merge dynamically later in their life. In this scenario the BH spins would be randomly oriented, potentially leading to a low χ_{eff}, regardless of the individual BH spins.

2. The scenario presented here involves no dynamical interactions while the BBH evolves within the disk. We can calculate the interaction time between a BBH and a tertiary star with a randomly oriented orbit:

$$t = \frac{1}{n\sigma V}$$

$$\simeq 2 \left(\frac{n}{10^3 \text{ pc}^{-3}}\right)^{-1} \left(\frac{a}{100 \text{ au}}\right)^{-2} \left(\frac{v_k}{650 \text{ km s}^{-1}}\right)^{-1} \text{Myr},$$

where we have adopted a cross-section, σ, derived from the orbital separation, and an interaction velocity V corresponding to the Keplerian orbit of a BBH at a distance of ~ 1 pc from a $10^8 M_\odot$ SMBH. For a stellar density of 10^3 pc^{-3} and an orbital separation of 10^2 au, we find an interaction time of ≈ 2 Myr, shorter than a merger time of ≈ 10 Myr. These strong dynamical encounters can fundamentally alter the BBHs orbit, reorienting the orbital angular momentum vector, altering the orbital eccentricity, and even trading companions. However, from Figure 6, note that most of the mass accreted by a BH occurs when the orbital separation shrinks to $\lesssim 10$ AU, with a much longer interaction time.

3. The accretion flow studied here is initially laminar, while AGN disk models typically assumed some α viscosity that parameterizes the role of isotropic, turbulent eddies that permeate the AGN disk. The characteristic length-scale of an eddy is $\sim \alpha H$, and depending on the value of $\mathcal{M}_w$, this can be comparable to R_b. If so, the evolution of the embedded binary could be driven more strongly by the accretion of eddies with randomly distributed angular momenta than by the angular momentum supplied from the AGN disk velocity profile. If this is the case, mass accretion might occur similarly, but the spin evolution of the binaries would be stochastic. This is, however, a different flow geometry than studied here and deserves attention in its own right.

While the relative importance of AGN disks as a formation scenario for BBH mergers may remain unresolved even after future LIGO/Virgo observing runs, the space-based gravitational wave detector LISA will be sensitive to BBHs in AGN. Although many different factors can impact the overall rate of systems observed by LISA, at sufficiently small orbital separations where gravitational wave radiation dominates the orbital evolution of point masses such as BBHs, general relativity makes a clear prediction for the distribution of BBH orbital separations, $P(a)$; since the strength of gravitational wave radiation increases with decreasing orbital separation, $(\dot{a}/a)_{\mathrm{GR}} \sim a^{-4}$ (Peters 1964), a population of equal-mass BBH binaries will have $P(a) \sim a^3$. However, at sufficiently large separations gas drag forces will dominate. Equation 14 indicates that $(\dot{a}/a)_{\mathrm{drag}}$ has no dependence on a when $a \ll R_b$, producing an orbital separation distribution $P(a) \sim a^{-1}$. By equating these two forces, we can find the critical orbital separation, a_{crit}, indicating the transition between the two regimes:

$$
\begin{aligned}
a_{\mathrm{crit}} \simeq 0.1 &\left(\frac{m_1}{30\, M_\odot}\right)^2 \left(\frac{c_\infty}{20\ \mathrm{km\ s^{-1}}}\right)^3 \\
&\times \left(\frac{\rho_\infty}{10^{-11}\ \mathrm{g\ cm^{-3}}}\right)^{-1} R_\odot.
\end{aligned}
\tag{21}
$$

This value is, however, derived using the purely hydrodynamic drag rate. As discussed in Section 4.2, most embedded BBHs will merge while accreting at super-Eddington rates, which can limit the efficiency of drag. To conservatively estimate a_{crit}, we can assume that drag is inversely dependent on the Eddington ratio, which implies that all mass ejected by super-Eddington outflows is done so at large radii relative to the binary separation. However, since $(\dot{a}/a)_{\mathrm{drag}}$ does not depend on a at small separations (Eq. 14), then $a_{\mathrm{crit}} \propto (\dot{a}/a)_{\mathrm{drag}}^{1/4}$. In the most extreme cases when the Eddington ratio reaches values $\sim 10^5$ (e.g., at distances ~ 0.1 pc in Fig. 5), then a_{crit} only increases by about a factor of ≈ 20. For two $30\, M_\odot$ BHs, this corresponds to an orbital period $\approx$ minutes (hours) or a gravitational wave frequency of $\approx 10^{-1}$ ($10^{-2} - 10^{-3}$) Hz for $a_{\mathrm{crit}} = 0.1$ (2) $R_\odot$, well within the LISA sensitivity band. We note that in the Toomre-stabilized regions of the AGN disk, gas density exhibits a steep dependence on the radius: $\rho_\infty \propto D^{-3}$ (Sirko & Goodman 2003). A density of 10^{-11} g cm^{-3} is appropriate for a BBH that is born at a distance of 10^{-1} pc, then merges at a distance of $\lesssim 10^{-2}$ pc from the AGN (e.g., light red trajectory in leftmost panel of Fig. 6). However, systems that initiate their evolution at larger distances from the AGN (dark red trajectories in Fig. 6) will merge at distances of $\gtrsim 1$ pc from the AGN, with gas densities $\approx 10^{-17}$ g cm^{-3} (at large radii, the sound speed is roughly constant in the S-G disk model). The corresponding a_{crit} in Equation 21 will therefore be too large for LISA to detect (the effect of gas accretion on the orbit is subdominant compared with gravitational wave radiation). While a complete analysis would quantitatively include the LISA sensitivity curve and a distribution of BH masses, our results indicate that for BBHs born sufficiently close to the AGN ($\lesssim 0.1$ pc), LISA ought to be able to observe the transition between the two power-law regimes.

5.2. *Electromagnetic signatures*

In recent years, the possibility that BBH mergers may be accompanied by electromagnetic (EM) signatures has intrigued the astrophysics community. There have been many proposed mechanisms for producing a signature, including the rapid accretion of relic disks post-merger (Perna et al. 2016; Schröder et al. 2018, Schröder et al. 2021 in prep), the shock-heating of circumbinary disks due to the post-merger recoil (Corrales et al. 2010; de Mink & King 2017), and mergers following a single-star progenitor (D'Orazio & Loeb

2018). In Bartos et al. (2017), they also studied the fates of embedded BBHs, and argued that these binaries could produce observable signatures by reaching super-Eddington luminosities via relativistic, beamed outflows. Interest in this scenario has been reinvigorated by the claimed association of an AGN flare with BBH merger GW190521. While this claim is tenuous (Ashton et al. 2020), it highlights one of the difficulties of this scenario: even if an embedded BBH produces a luminous signal, it must be distinguished from the dominant AGN emission.

Radiation may be produced by an embedded BBH either by accretion during the inspiral phase or transiently immediately following the merger. We turn our attention, first, to the case of a steady-state luminosity. In many cases, including the evolutionary tracks depicted in Figure 5, the embedded BBH is supplied[2] gas at rates near the Eddington limit or significantly above it (as pointed out by other authors, e.g., Stone et al. 2017; Bartos et al. 2017). However, even in cases where the mass accretion rate can exceed the Eddington limit, the luminosity itself will still be limited because radiation becomes trapped within the flow. In this case, the accretion flow will be a geometrically and optically thick advection-dominated accretion flow ('ADAF', Narayan & Yi 1994), producing an unusually soft blackbody spectrum. For an Eddington-limited pair of stellar-mass black holes to be observable, they must compete with the host AGN. The relative luminosity of the BBH accretor to the AGN is,

$$\frac{L_{\rm BBH}}{L_{\rm AGN}} \sim 10^{-7} \left(\frac{\lambda_{\rm Edd}^{\rm (SMBH)}}{0.1}\right) \left(\frac{M}{60\,M_\odot}\right) \left(\frac{M_{\rm SMBH}}{10^8\,M_\odot}\right)^{-1} \quad (22)$$

For typical values of $\lambda_{\rm Edd}^{\rm (SMBH)}$, $M_{\rm BBH}$, and $M_{\rm SMBH}$, this value is extremely small and the accreting BBH will be indistinguishable from the host AGN unless the two are resolved.

Clearly, if the electromagnetic signatures from an embedded BBH are to be observed, it must shine brighter than the Eddington luminosity. The most natural way for this to happen is by producing a collimated, relativistic jet that has its emission beamed towards us (e.g., MacLeod et al. 2014). We can estimate an upper limit on the jet luminosity by assuming the flow is magnetically arrested, producing powerful Blandford-Znajek jets due to large poloidal magnetic fields (Blandford & Znajek 1977; Tchekhovskoy et al. 2011). Assuming this, we take

$$L_{\rm jet} = \eta_{\rm MAD}\dot{M}c^2 \quad (23)$$

where $\eta_{\rm MAD}$ is the jet efficiency for a magnetically arrested disk (MAD). The jet efficiency in MADs commonly reaches

$\sim 200-300\%$ by tapping the rotational energy of the BH (Tchekhovskoy et al. 2011), so we assume a characteristic $\eta_{\rm MAD} = 2$. Assuming that the radiative efficiency of the accretion flow is $\eta \approx 0.1$, then the total jet luminosity is

$$L_{\rm jet} \approx 20 \left(\frac{\eta_{\rm MAD}}{2}\right) \left(\frac{\eta}{0.1}\right)^{-1} L_{\rm Edd} \quad (24)$$

If this jet is directed towards us, the emission will be beamed within an opening angle $\theta \sim 1/\Gamma$, where Γ is the Lorentz factor of the jet. If we measure the flux from this jet at earth, then the inferred isotropic luminosity is,

$$L_{\rm iso} \sim \frac{4\pi}{\theta^2}\frac{L_{\rm jet}}{2} = \Gamma^2 2\pi L_{\rm jet} \quad (25)$$

If we compare this boosted luminosity to the host AGN luminosity, then we find that

$$\frac{L_{\rm iso}}{L_{\rm AGN}} \sim 10^{-5}\Gamma^2 \left(\frac{2}{\eta_{\rm MAD}}\right) \left(\frac{0.1}{\eta}\right)^{-1} \left(\frac{\lambda_{\rm Edd}^{\rm (SMBH)}}{0.1}\right)$$
$$\times \left(\frac{M}{60\,M_\odot}\right) \left(\frac{M_{\rm SMBH}}{10^8\,M_\odot}\right)^{-1} \quad (26)$$

If we require that $L_{\rm iso} \gtrsim L_{\rm AGN}$, then the corresponding Γ for which this is achieved is $\Gamma \approx 316$. This is in the upper range of Γ values associated with gamma-ray bursts (Lithwick & Sari 2001; Gehrels et al. 2009), and corresponds to an opening angle $\theta \sim 0.18°$. Even if embedded BBHs could produce jets with this Lorentz factor, we would only see $\times \theta^2/4 \sim 0.0002\%$ of them due to the inclination-dependence of the emission. Furthermore, while Bartos et al. (2017) suggest that embedded BBHs form gaps, allowing jets to escape unimpeded, Fig. 2 suggests most binaries will not form gaps, and Fig. 5 suggests most binaries merge in the outer regions ($\gtrsim 0.1-1\,{\rm pc}$) of the disk. In these regions, $\mathcal{M}_{\rm w} \sim 0.1$, and H is roughly two orders of magnitude larger than the binary sphere of influence. This provides a large column density of material for the jet to traverse, likely resulting in significant mass-loading which would lower the resulting Γ. This suggests that it is difficult to detect a jet associated with an embedded BBH unless it occurs at frequencies separate from the dominant AGN emission. We note that the EM signatures associated with these jets have been studied in detail by two recent papers; Zhu et al. (2021), for the case of embedded neutron stars, and Perna et al. (2021), for jet propagation from both BHs and neutron stars. In both works, they emphasize the issue of distinguishing the transient emission from the AGN emission, and find that the transient can more easily outshine the AGN in the X-ray, infrared and radio bands.

Finally, we consider the possibility of transient EM signatures that occur during or immediately following merger. There are two possibilities; the first possibility is that the binary experiences a transient spike in its accretion rate

---

[2] We intentionally avoid the term *accreted*, here, because while we can confidently estimate the gas supply rate via Equation 12, the actual fraction of accreted material on sub-grid scales is uncertain.

and thus luminosity post-merger (Milosavljević & Phinney 2005). However, these studies were focused on thin circumbinary disks with carved out cavities, and in the thick flows that accompany these binaries no such spike is likely to exist. We therefore ignore this possibility. The other possibility is that the sudden decrease in gravitational potential at the onset of merger rapidly shocks the surrounding gaseous envelope, producing intense photospheric emission.

The sudden mass loss accompanying the BBH merger is associated with a drop of potential energy in the surrounding high-density envelope,

$$\Delta E = \int_{R_{\rm bw}} \frac{G\Delta M_{\rm merger}}{r}\rho(r)dV \tag{27}$$

We assume that within the BBH sphere of influence, characterized by $R_{\rm bw}$ (Eq. 11), the density profile is Bondi-like, i.e. $\rho(r) \sim \rho_\infty(r/R_{\rm bw})^{-3/2}$ (Shapiro & Teukolsky 1983). This yields a change in potential energy,

$$\Delta E = 4\pi\rho_\infty G\Delta M_{\rm merger}R_{\rm bw}^2 \tag{28}$$

If we assume the flow is Bondi-like in the region of interest and that roughly $\sim 50\%$ of the BBH mass is lost upon merger, then this change in energy can be rewritten as,

$$\Delta E \approx 8.1 \times 10^{40}\,{\rm ergs}\left(\frac{M}{60M_\odot}\right)^3\left(\frac{\rho_\infty}{10^{-18}\,{\rm g\,cm^{-3}}}\right)$$
$$\times \left(\frac{c_\infty}{25\,{\rm km\,s^{-1}}}\right)^{-4} \tag{29}$$

If we crudely assume that this energy is lost within a sound-crossing time $\Delta t = R_{\rm b}/c_\infty$, then the luminosity produced by the shock ($\approx \Delta E/\Delta t$) is

$$L_{\rm shock} \approx 1.6 \times 10^{32}\,{\rm ergs\,s^{-1}}\quad\left(\frac{M}{60M_\odot}\right)^2\left(\frac{\rho_\infty}{10^{-18}\,{\rm g\,cm^{-3}}}\right)$$
$$\times \left(\frac{c_\infty}{25\,{\rm km\,s^{-1}}}\right)^{-1} \tag{30}$$

Since a near-Eddington, $10^8\,M_\odot$ host SMBH should have a luminosity of roughly $L_{\rm AGN} \approx 10^{45} - 10^{46}\,{\rm ergs\,s^{-1}}$, it is implausible for the luminosity of the post-merger shock to exceed that of the AGN.

5.3. *Feedback*

One of the uncertainties in the accretion flow embedding the binaries is the role of feedback. Feedback can be deposited into the gas supply either radiatively or mechanically, through winds and relativistic jets, and can effect the mass accretion rate and efficiency of drag.

If an accreting binary produces a jet, it is possible for the jet to carve out a cavity and suppress the gas supply (e.g. Ramirez-Ruiz et al. 2002). If the force exerted on the ambient medium by a relativistic jet $\sim L_{\rm jet}/c$, then it will exert a ram pressure $\sim L_{\rm jet}/c\theta^2 r^2$, where θ is the opening angle of the jet. By assuming that as the jet plunges through the medium, it becomes subrelativistic and spreads laterally, we can take $\theta^2 = 4\pi$. We can set the jet ram pressure equal to the gas pressure of the ambient medium to determine the radius of the jet-medium interface (denoted r_j),

$$\frac{L_{\rm jet}}{4\pi r_j^2 c} = \rho_\infty c_\infty^2,$$
$$r_j = \sqrt{\frac{L_{\rm jet}}{4\pi\rho_\infty c_\infty^2 c}} \tag{31}$$

To compare this to the relevant physical scale, we can write r_j in terms of the Bondi radius and physical values,

$$r_j/R_{\rm b} \approx 56\left(\frac{\lambda_{\rm Edd}^{\rm (jet)}}{20}\right)^{1/2}\left(\frac{M}{60M_\odot}\right)^{-1/2}$$
$$\times \left(\frac{\rho_\infty}{10^{-18}\,{\rm g\,cm^{-3}}}\right)^{-1/2}\left(\frac{c_\infty}{25\,{\rm km\,s^{-1}}}\right) \tag{32}$$

In this relation, we've expressed the jet luminosity in terms of its Eddington ratio, $\lambda_{\rm Edd}^{\rm (jet)}$. For the assumed ambient conditions (typical of the AGN disk at $\approx 1\,{\rm pc}$) and Eddington ratio (an upper limit, see Eq. 24), r_j is much larger than $R_{\rm b}$. This suggests that if a powerful jet is produced by the binary, it should easily carve out a large cavity and impede gas supply. This could at least transiently diminish the accretion rate and may impose a duty cycle on the growth of the BBH. Alternatively, we can use $r_j < R_{\rm B}$ as the condition required for a cavity not to form. Then, the maximum Eddington ratio of the jet is,

$$\lambda_{\rm Edd}^{\rm (jet)} < 0.0064\left(\frac{M}{60M_\odot}\right)\left(\frac{\rho_\infty}{10^{-18}\,{\rm g\,cm^{-3}}}\right)\left(\frac{c_\infty}{25\,{\rm km\,s^{-1}}}\right)^{-2} \tag{33}$$

This is an extremely low jet efficiency and would likely require a black hole with a very small spin (Narayan et al. 2003). However, closer to $\approx 10^{-1} - 10^{-2}\,{\rm pc}$, the gas density can reach $\approx 10^{-14}\,{\rm g\,cm^{-3}}$ (Sirko & Goodman 2003), which would result in a minimum Eddington ratio of 64. This suggests that the ability of a jet to impede the gas supply strongly depends on where the BBH is in the disk; at larger distances, it likely induces a duty cycle in the accretion flow, while at smaller distances the jet will be quickly extinguished.

5.4. *Caveats*

The results of this work, particularly the evolutionary tracks laid out in Section 4.2, have uncertainties that deserve emphasis. Here are a few essential ingredients required to properly understand the evolution of embedded BBHs:

- Understanding how drag and mass accretion rates change in the super-Eddington regime is critical to

understanding the evolution of embedded BBHs. The ratio of the accretion to inspiral timescale is what determines the final mass of the binary upon merger and will be altered if radiation is realistically taken into account. Additionally, the radiative efficiency affects both the mass accretion rate and the evolutionary timescale. While we use a constant radiative efficiency of $\eta = 0.01$, it will be higher in the sub-Eddington regime, but can be even lower in the highly super-Eddington regime. While the details of the evolutionary tracks depend on how drag in the super-Eddington regime is prescribed, two main features are clear: that embedded BBHs can grow significantly, possibly entering the PISN mass gap before merging, and that the time-to-merger is $\lesssim 5 - 30\,\mathrm{Myr}$.

- The true nature of AGN disks, particularly in the outer Toomre-unstable region, remains an open question. While we favor the profiles of Sirko & Goodman (2003), they use an unspecified pressure source to stabilize this region. This provides a useful model for making predictions but remains a crude estimate which should be explored further. Additionally, as discussed in Section 4.2, the time-dependence of AGN disks is a major uncertainty. As found in the simulations of Angles-Alcazar et al. (2020), at parsec scales the disk can reorient itself on $\approx\,\mathrm{Myr}$ timescales, which may alter the occupation fraction of black holes in the AGN disk or limit the total amount of time the binaries have to evolve in the disk.

- We assumed that the embedded BBH is allowed to evolve through the AGN undisturbed, but in reality it dynamically couples to the surrounding stellar population. Three-body scattering may merge the BBH faster (Stone et al. 2017) or may reorient the binaries with respect to the surrounding flow, which can alter the mass and spin evolution of the binaries prior to merger. Additionally, as discussed in Section 4.1, a proper understanding of the black hole distribution near the SMBH will allow us to better understand how many BHs can be captured dynamically by the AGN and where their initial position in the disk is, which can strongly affect their subsequent evolution.

5.5. *Summary*

To summarize, we describe the chronology of embedded BBHs as they evolve hydrodynamically through the host AGN disk:

- *Birth.* A pair of black holes are either born in the disk (typically $\gtrsim 0.1 - 1\,\mathrm{pc}$), or they are dynamically captured. If the nuclear cluster harbors a black hole cusp, it is possible for the black holes to be initially captured

at much smaller radii. As discussed in Section 4.1, it is unclear whether or not a black hole cusp will have been formed during the AGN phase of the SMBH, particularly for higher mass SMBHs where the relaxation timescale of the surrounding stellar population can be longer than the age of the Universe. For this reason, we find it more likely that BBHs first become embedded in the outer regions of the AGN disk.

- *Accretion.* As an embedded BBH orbits prograde with the AGN disk, it will become engulfed in a gaseous wind that has an asymmetric velocity profile in the rest frame of the BBH. This is depicted in Figures 1, 2 and 3, where the characteristics of the accretion flow are primarily defined by $\mathcal{M}_\mathrm{w}$, the Mach number of the wind in the BBH rest frame. At large $\mathcal{M}_\mathrm{w}$, the ram pressure of the wind dominates the accretion flow, and at small $\mathcal{M}_\mathrm{w}$ the accretion flow becomes Bondi-like. In the outer, Toomre unstable regions of an AGN disk, $\mathcal{M}_\mathrm{w}$ is often small enough that Bondi accretion provides an adequate approximation (Fig. 2). When $\mathcal{M}_\mathrm{w}$ is large enough ($\gg 1$), the accretion flow becomes planar, likely resembling a pair of thin mini-disks and potentially opening a cavity in the AGN disk (Baruteau et al. 2011; Li et al. 2021). Our analysis is invalid in this regime, which likely holds for AGN disks that are geometrically thin and are hosted by lighter ($\sim 10^6\,M_\odot$) SMBHs. This makes our results most salient for binaries embedded within the disks of heavier ($\gtrsim 10^7\,M_\odot$) SMBHs. For most regions in the disk, a BBH will accrete at super-Eddington rates (Section 4.2); if the BBH accretes at the Eddington limit for $\gtrsim 5\,\mathrm{Myr}$, it can double its mass.

- *Inspiral.* The inspiral of the BBH is most strongly governed by mass accretion and drag, with drag contributing slightly more than mass accretion (Fig. 4). In Section 3.3, we provide analytic expressions with best-fit numerical coefficients that reasonably reproduce the inspiral rate measured in our hydrodynamic simulations. We find that typical BBHs, beginning their journey anywhere between 0.1 and 2 pc in the AGN disk, will merge within $\approx 5 - 30\,\mathrm{Myr}$.

- *Migration.* Concurrent to accretion and inspiral, embedded BBHs will migrate in the AGN disk (typically inwards). We find that BBHs that start at large distances from the AGN ($\gtrsim 1 - 2\,\mathrm{pc}$) may migrate only marginally, while BBHs beginning at $\lesssim 0.1 - 1\,\mathrm{pc}$ can migrate to $10^{-3} - 10^{-2}\,\mathrm{pc}$ before merging.

- *Multimessenger signatures.* In Section 4, we found that BBHs can often double their mass during their inspiral. This can alter the resulting black hole

mass spectrum detected by LIGO, allowing embedded BBHs to enter the pair-instability supernova mass gap, as discussed in Section 5.1. In Section 5.2, we studied the possible EM signatures accompanying an accreting BBH or occurring transiently post-merger. In general, it is difficult for the BBH to outshine its host AGN. If the BBH produced a relativistic jet, it would have to have a large Lorentz factor to be detectable, leaving only a very small fraction of these sources detectable due to the inclination-dependence of the beamed emission. Shock heating in the AGN disk due to the post-merger recoil can produce electromagnetic transients, but with luminosities far less than that of the AGN.

ACKNOWLEDGEMENTS

APPENDIX

A. SIMULATION CONVERGENCE

In our simulations, we represented the boundaries of the black holes with an absorbing boundary condition of radius $R_s = 0.0125 R_b$. In Figure 7, we show the convergence of our accretion and inspiral rates as a function of R_s by comparing them at $R_s = 0.0625, 0.0125$ and $0.025 R_b$. A full simulation run at $R_s = 0.0625 R_b$ is computationally expensive, so we opted to restart the $R_s = 0.0125 R_b$ simulation at $t = 40 R_b/c_\infty$ (well into steady state) and run it for 10 accretion timescales. For $R_s = 0.0625 R_b$, we also increased the maximum AMR level so the number of cells across a sink radius would remain constant. We used this restart approach for $R_s = 0.025 R_b$ as well, and also compared it to running the full simulation duration at that sink radius, and found no difference in the result. In the specific case of Fig. 7, we used the simulation with $a = 0.1 R_b$ and $\mathcal{M}_w = 0.5$. We find that that the accretion rate typically decreases with sink radius and that the inspiral rate is relatively constant albeit with higher variability at smaller sink radii. This is expected; as the sink radius decreases, more streamlines are deflected before reaching the boundary, decreasing the accretion rate (e.g., Xu & Stone 2019). On the other hand, gravitational drag results from the cumulative influence of all gas in the binary's sphere of influence, and so is less sensitive to the sink radius. This suggests that our results regarding drag in Section 3.3 should be relatively robust, but the mass accretion rate should be taken as an upper limit.

In Figure 8, we plot the accretion and inspiral rates for the majority of the simulation run-time for each simulation (excluding the intermediate $\mathcal{M}_w = 1$ simulations). In general, both are highly variable, so we opted to plot averages over both quantities in $t = 4 R_b/c_\infty$ bins. We depict both rates at times $> 20 R_b/c_\infty$, after transient spikes in the accretion and inspiral rates have died off and the flow reaches steady state.

REFERENCES

Abbott, B. P., Abbott, R., Abbott, T. D., et al. 2019, Physical Review X, 9, 031040, doi: 10.1103/PhysRevX.9.031040

Abbott, R., Abbott, T. D., Abraham, S., et al. 2020a, ApJL, 896, L44, doi: 10.3847/2041-8213/ab960f

—. 2020b, ApJL, 900, L13, doi: 10.3847/2041-8213/aba493

Abbott, R., Abbott, T. D., Abraham, S., et al. 2020, Phys. Rev. Lett., 125, 101102, doi: 10.1103/PhysRevLett.125.101102

Abbott, R., Abbott, T. D., Abraham, S., et al. 2020, ApJL, 900, L13, doi: 10.3847/2041-8213/aba493

Alexander, T., & Hopman, C. 2009, ApJ, 697, 1861, doi: 10.1088/0004-637X/697/2/1861

Angles-Alcazar, D., Quataert, E., Hopkins, P., et al. 2020, arXiv e-prints, arXiv:2008.12303. https://arxiv.org/abs/2008.12303

Antoni, A., MacLeod, M., & Ramirez-Ruiz, E. 2019, ApJ, 884, 22, doi: 10.3847/1538-4357/ab3466

Antonini, F. 2014, ApJ, 794, 106, doi: 10.1088/0004-637X/794/2/106
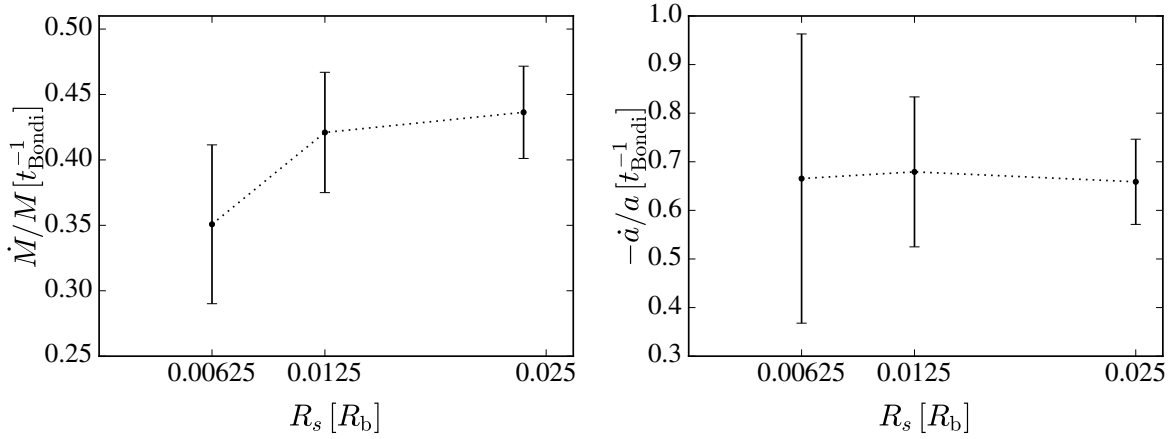
Figure 7. We plot the time-averaged accretion and inspiral rates for different sink radii in our $a = 0.1 R_{\rm b}$, $\mathcal{M}_{\rm w} = 0.5$ simulation. $R_{\rm s} = 0.0125 R_{\rm b}$ was the value standardly used in our simulations. $R_{\rm s} = 0.00625 R_{\rm b}$ is computationally expensive, as it requires increasing the resolution to resolve the boundary adequately, so this simulation was restarted from the $R_{\rm s} = 0.0125 R_{\rm b}$ run at $t = 40 R_{\rm b}/c_\infty$ and ran for 10 more accretion timescales. For $R_{\rm s} = 0.025 R_{\rm b}$, we ran both a full simulation and one restarted at $t = 40 R_{\rm b}/c_\infty$, and both resulted in the same average accretion and inspiral rates.
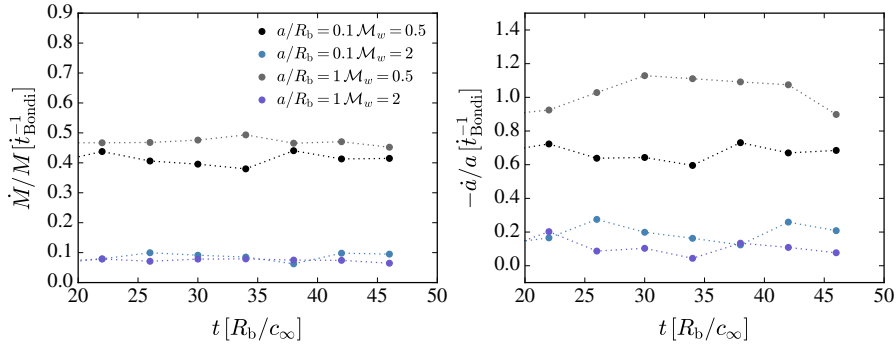
Figure 8. We plot the accretion and inspiral rates for several of our simulations for the majority of the simulation run-time. Since these rates have strong variability, we averaged both quantities in $4 R_{\rm b}/c_\infty$ bins, represented by each scatter point. The plots depict times $> 20 R_{\rm b}/c_\infty$ after which the flow is in quasi-steady state.

Antonini, F., Barausse, E., & Silk, J. 2015, ApJ, 812, 72, doi: 10.1088/0004-637X/812/1/72

Antonini, F., & Perets, H. B. 2012, ApJ, 757, 27, doi: 10.1088/0004-637X/757/1/27

Antonini, F., Toonen, S., & Hamers, A. S. 2017, ApJ, 841, 77, doi: 10.3847/1538-4357/aa6f5e

Ashton, G., Ackley, K., Magaña Hernand ez, I., & Piotrzkowski, B. 2020, arXiv e-prints, arXiv:2009.12346. https://arxiv.org/abs/2009.12346

Askar, A., Szkudlarek, M., Gondek-Rosińska, D., Giersz, M., & Bulik, T. 2017, MNRAS, 464, L36, doi: 10.1093/mnrasl/slw177

Bahcall, J. N., & Wolf, R. A. 1976, ApJ, 209, 214, doi: 10.1086/154711

Banerjee, S. 2018, MNRAS, 473, 909, doi: 10.1093/mnras/stx2347

Bartko, H., Martins, F., Fritz, T. K., et al. 2009, ApJ, 697, 1741, doi: 10.1088/0004-637X/697/2/1741

Bartko, H., Martins, F., Trippe, S., et al. 2010, ApJ, 708, 834, doi: 10.1088/0004-637X/708/1/834

Bartos, I., Kocsis, B., Haiman, Z., & Márka, S. 2017, ApJ, 835, 165, doi: 10.3847/1538-4357/835/2/165

Baruteau, C., Cuadra, J., & Lin, D. N. C. 2011, ApJ, 726, 28, doi: 10.1088/0004-637X/726/1/28

Bavera, S. S., Fragos, T., Zevin, M., et al. 2020, arXiv e-prints, arXiv:2010.16333. https://arxiv.org/abs/2010.16333

Belczynski, K. 2020, arXiv e-prints, arXiv:2009.13526. https://arxiv.org/abs/2009.13526

Belczynski, K., Holz, D. E., Bulik, T., & O'Shaughnessy, R. 2016, Nature, 534, 512, doi: 10.1038/nature18322

Blandford, R. D., & Znajek, R. L. 1977, MNRAS, 179, 433, doi: 10.1093/mnras/179.3.433

Blondin, J. M., & Raymer, E. 2012, ApJ, 752, 30, doi: 10.1088/0004-637X/752/1/30

Bondi, H. 1952, MNRAS, 112, 195, doi: 10.1093/mnras/112.2.195

Corrales, L. R., Haiman, Z., & MacFadyen, A. 2010, MNRAS, 404, 947, doi: 10.1111/j.1365-2966.2010.16324.x

Dai, L., McKinney, J. C., Roth, N., Ramirez-Ruiz, E., & Miller, M. C. 2018, ApJL, 859, L20, doi: 10.3847/2041-8213/aab429

De, S., MacLeod, M., Everson, R. W., et al. 2020, ApJ, 897, 130, doi: 10.3847/1538-4357/ab9ac6

de Mink, S. E., & King, A. 2017, ApJL, 839, L7, doi: 10.3847/2041-8213/aa67f3

Di Carlo, U. N., Giacobbo, N., Mapelli, M., et al. 2019, MNRAS, 487, 2947, doi: 10.1093/mnras/stz1453

D'Orazio, D. J., & Loeb, A. 2018, PhRvD, 97, 083008, doi: 10.1103/PhysRevD.97.083008

Edgar, R. 2004, NewAR, 48, 843, doi: 10.1016/j.newar.2004.06.001

Everson, R. W., MacLeod, M., De, S., Macias, P., & Ramirez-Ruiz, E. 2020, ApJ, 899, 77, doi: 10.3847/1538-4357/aba75c

Federrath, C., Banerjee, R., Clark, P. C., & Klessen, R. S. 2010, ApJ, 713, 269, doi: 10.1088/0004-637X/713/1/269

Fragione, G., & Kocsis, B. 2018, PhRvL, 121, 161103, doi: 10.1103/PhysRevLett.121.161103

Frank, J., King, A., & Raine, D. J. 2002, Accretion Power in Astrophysics: Third Edition

French, K. D., Wevers, T., Law-Smith, J., Graur, O., & Zabludoff, A. I. 2020, SSRv, 216, 32, doi: 10.1007/s11214-020-00657-y

Fryxell, B., Olson, K., Ricker, P., et al. 2000, ApJS, 131, 273, doi: 10.1086/317361

Gehrels, N., Ramirez-Ruiz, E., & Fox, D. B. 2009, ARA&A, 47, 567, doi: 10.1146/annurev.astro.46.060407.145147

Ghez, A. M., Duchêne, G., Matthews, K., et al. 2003, ApJL, 586, L127, doi: 10.1086/374804

Giacobbo, N., & Mapelli, M. 2018, MNRAS, 480, 2011, doi: 10.1093/mnras/sty1999

Goodman, J. 2003, MNRAS, 339, 937, doi: 10.1046/j.1365-8711.2003.06241.x

Graham, M. J., Ford, K. E. S., McKernan, B., et al. 2020, PhRvL, 124, 251102, doi: 10.1103/PhysRevLett.124.251102

Hailey, C. J., Mori, K., Bauer, F. E., et al. 2018, Nature, 556, 70, doi: 10.1038/nature25029

Heckman, T. M., & Best, P. N. 2014, ARA&A, 52, 589, doi: 10.1146/annurev-astro-081913-035722

Kaaz, N., Antoni, A., & Ramirez-Ruiz, E. 2019, ApJ, 876, 142, doi: 10.3847/1538-4357/ab158b

Kaaz, N., Kremer, K., Auchettl, K., & Ramirez-Ruiz, E. 2020, arXiv e-prints, arXiv:2002.09502. https://arxiv.org/abs/2002.09502

King, A. R., & Begelman, M. C. 1999, ApJL, 519, L169, doi: 10.1086/312126

King, A. R., Pringle, J. E., & Livio, M. 2007, MNRAS, 376, 1740, doi: 10.1111/j.1365-2966.2007.11556.x

Kremer, K., Chatterjee, S., Ye, C. S., Rodriguez, C. L., & Rasio, F. A. 2019, ApJ, 871, 38, doi: 10.3847/1538-4357/aaf646

Kremer, K., Ye, C. S., Chatterjee, S., Rodriguez, C. L., & Rasio, F. A. 2018, ApJL, 855, L15, doi: 10.3847/2041-8213/aab26c

Kruckow, M. U., Tauris, T. M., Langer, N., Kramer, M., & Izzard, R. G. 2018, MNRAS, 481, 1908, doi: 10.1093/mnras/sty2190

Law-Smith, J., Ramirez-Ruiz, E., Ellison, S. L., & Foley, R. J. 2017, ApJ, 850, 22, doi: 10.3847/1538-4357/aa94c7

Leigh, N. W. C., Geller, A. M., McKernan, B., et al. 2018, MNRAS, 474, 5672, doi: 10.1093/mnras/stx3134

Li, Y.-P., Dempsey, A. M., Li, S., Li, H., & Li, J. 2021, arXiv e-prints, arXiv:2101.09406. https://arxiv.org/abs/2101.09406

Lippai, Z., Frei, Z., & Haiman, Z. 2008, ApJL, 676, L5, doi: 10.1086/587034

Lithwick, Y., & Sari, R. 2001, ApJ, 555, 540, doi: 10.1086/321455

Lu, J. R., Ghez, A. M., Hornstein, S. D., et al. 2009, ApJ, 690, 1463, doi: 10.1088/0004-637X/690/2/1463

Lyra, W., Paardekooper, S.-J., & Mac Low, M.-M. 2010, ApJL, 715, L68, doi: 10.1088/2041-8205/715/2/L68

MacLeod, M., Antoni, A., Murguia-Berthier, A., Macias, P., & Ramirez-Ruiz, E. 2017, ApJ, 838, 56, doi: 10.3847/1538-4357/aa6117

MacLeod, M., Goldstein, J., Ramirez-Ruiz, E., Guillochon, J., & Samsing, J. 2014, ApJ, 794, 9, doi: 10.1088/0004-637X/794/1/9

MacLeod, M., & Ramirez-Ruiz, E. 2015a, ApJ, 803, 41, doi: 10.1088/0004-637X/803/1/41

—. 2015b, ApJL, 798, L19, doi: 10.1088/2041-8205/798/1/L19

McKernan, B., Ford, K. E. S., Kocsis, B., Lyra, W., & Winter, L. M. 2014, MNRAS, 441, 900, doi: 10.1093/mnras/stu553

McKernan, B., Ford, K. E. S., Lyra, W., & Perets, H. B. 2012, MNRAS, 425, 460, doi: 10.1111/j.1365-2966.2012.21486.x

McKernan, B., Ford, K. E. S., Bellovary, J., et al. 2018, ApJ, 866, 66, doi: 10.3847/1538-4357/aadae5

McKernan, B., Ford, K. E. S., Bartos, I., et al. 2019, ApJL, 884, L50, doi: 10.3847/2041-8213/ab4886

McKinney, J. C., Dai, L., & Avara, M. J. 2015, MNRAS, 454, L6, doi: 10.1093/mnrasl/slv115

McKinney, J. C., Tchekhovskoy, A., Sadowski, A., & Narayan, R. 2014, MNRAS, 441, 3177, doi: 10.1093/mnras/stu762

Milosavljević, M., & Phinney, E. S. 2005, ApJL, 622, L93, doi: 10.1086/429618

Mockler, B., & Ramirez-Ruiz, E. 2021, ApJ, 906, 101, doi: 10.3847/1538-4357/abc955

Morris, M. 1993, ApJ, 408, 496, doi: 10.1086/172607

Muñoz, D. J., Lai, D., Kratter, K., & Mirand a, R. 2020, ApJ, 889, 114, doi: 10.3847/1538-4357/ab5d33

Muñoz, D. J., Miranda, R., & Lai, D. 2019, ApJ, 871, 84, doi: 10.3847/1538-4357/aaf867

Murguia-Berthier, A., MacLeod, M., Ramirez-Ruiz, E., Antoni, A., & Macias, P. 2017, ApJ, 845, 173, doi: 10.3847/1538-4357/aa8140

Narayan, R., Igumenshchev, I. V., & Abramowicz, M. A. 2003, PASJ, 55, L69, doi: 10.1093/pasj/55.6.L69

Narayan, R., & Yi, I. 1994, ApJL, 428, L13, doi: 10.1086/187381

O'Leary, R. M., Kocsis, B., & Loeb, A. 2009, MNRAS, 395, 2127, doi: 10.1111/j.1365-2966.2009.14653.x

Paardekooper, S. J. 2014, MNRAS, 444, 2031, doi: 10.1093/mnras/stu1542

Paardekooper, S. J., Baruteau, C., Crida, A., & Kley, W. 2010, MNRAS, 401, 1950, doi: 10.1111/j.1365-2966.2009.15782.x

Paardekooper, S. J., Baruteau, C., & Kley, W. 2011, MNRAS, 410, 293, doi: 10.1111/j.1365-2966.2010.17442.x

Paumard, T., Genzel, R., Martins, F., et al. 2006, ApJ, 643, 1011, doi: 10.1086/503273

Perna, R., Lazzati, D., & Cantiello, M. 2021, ApJL, 906, L7, doi: 10.3847/2041-8213/abd319

Perna, R., Lazzati, D., & Giacomazzo, B. 2016, ApJL, 821, L18, doi: 10.3847/2041-8205/821/1/L18

Peters, P. C. 1964, Physical Review, 136, 1224, doi: 10.1103/PhysRev.136.B1224

Pringle, J. E. 1981, ARA&A, 19, 137, doi: 10.1146/annurev.aa.19.090181.001033

Ptak, A. 2001, in American Institute of Physics Conference Series, Vol. 599, X-ray Astronomy: Stellar Endpoints, AGN, and the Diffuse X-ray Background, ed. N. E. White, G. Malaguti, & G. G. C. Palumbo, 326–335

Ramirez-Ruiz, E., Celotti, A., & Rees, M. J. 2002, MNRAS, 337, 1349, doi: 10.1046/j.1365-8711.2002.05995.x

Rasio, F. A., Freitag, M., & Gürkan, M. A. 2004, in Coevolution of Black Holes and Galaxies, ed. L. C. Ho, 138

Rodriguez, C. L., Amaro-Seoane, P., Chatterjee, S., & Rasio, F. A. 2018, PhRvL, 120, 151101, doi: 10.1103/PhysRevLett.120.151101

Safarzadeh, M., Farr, W. M., & Ramirez-Ruiz, E. 2020a, ApJ, 894, 129, doi: 10.3847/1538-4357/ab80be

—. 2020b, ApJ, 894, 129, doi: 10.3847/1538-4357/ab80be

Samsing, J., & D'Orazio, D. J. 2018, MNRAS, 481, 5445, doi: 10.1093/mnras/sty2334

Samsing, J., MacLeod, M., & Ramirez-Ruiz, E. 2014, ApJ, 784, 71, doi: 10.1088/0004-637X/784/1/71

Samsing, J., & Ramirez-Ruiz, E. 2017, ApJL, 840, L14, doi: 10.3847/2041-8213/aa6f0b

Schawinski, K., Koss, M., Berney, S., & Sartori, L. F. 2015, MNRAS, 451, 2517, doi: 10.1093/mnras/stv1136

Schödel, R., Ott, T., Genzel, R., et al. 2002, Nature, 419, 694, doi: 10.1038/nature01121

Schröder, S. L., Batta, A., & Ramirez-Ruiz, E. 2018, ApJL, 862, L3, doi: 10.3847/2041-8213/aacf8d

Secunda, A., Bellovary, J., Mac Low, M.-M., et al. 2019, ApJ, 878, 85, doi: 10.3847/1538-4357/ab20ca

—. 2020, arXiv e-prints, arXiv:2004.11936. https://arxiv.org/abs/2004.11936

Shakura, N. I., & Sunyaev, R. A. 1973, A&A, 500, 33

Shapiro, S. L., & Teukolsky, S. A. 1983, Black holes, white dwarfs, and neutron stars : the physics of compact objects

Sirko, E., & Goodman, J. 2003, MNRAS, 341, 501, doi: 10.1046/j.1365-8711.2003.06431.x

Stone, N. C., Metzger, B. D., & Haiman, Z. 2017, MNRAS, 464, 946, doi: 10.1093/mnras/stw2260

Tagawa, H., Haiman, Z., & Kocsis, B. 2019, arXiv e-prints, arXiv:1912.08218. https://arxiv.org/abs/1912.08218

Tagawa, H., & Umemura, M. 2018, ApJ, 856, 47, doi: 10.3847/1538-4357/aab0a4

Tagawa, H., Umemura, M., & Gouda, N. 2016, MNRAS, 462, 3812, doi: 10.1093/mnras/stw1877

Tanaka, H., & Ward, W. R. 2004, ApJ, 602, 388, doi: 10.1086/380992

Tchekhovskoy, A., Narayan, R., & McKinney, J. C. 2011, MNRAS, 418, L79, doi: 10.1111/j.1745-3933.2011.01147.x

The LIGO Scientific Collaboration, the Virgo Collaboration, Abbott, R., et al. 2020, arXiv e-prints, arXiv:2004.08342. https://arxiv.org/abs/2004.08342

Thompson, T. A., Quataert, E., & Murray, N. 2005, ApJ, 630, 167, doi: 10.1086/431923

Toomre, A. 1964, ApJ, 139, 1217, doi: 10.1086/147861

Vigna-Gómez, A., Toonen, S., Ramirez-Ruiz, E., et al. 2021, ApJL, 907, L19, doi: 10.3847/2041-8213/abd5b7

Ward, W. R., & Hahn, J. M. 1994, Icarus, 110, 95, doi: 10.1006/icar.1994.1109

Xu, W., & Stone, J. M. 2019, MNRAS, 488, 5162, doi: 10.1093/mnras/stz2002

Zhu, J.-P., Zhang, B., Yu, Y.-W., & Gao, H. 2021, ApJL, 906, L11, doi: 10.3847/2041-8213/abd412